Corrigendum to: A review on silicene – New candidate for electronics

Article *in* Surface Science Reports · May 2012

Impact Factor: 14.77 · DOI: 10.1016/j.surfrep.2011.10.001

Surface Science Reports 67 (2012) 1–18

Contents lists available at SciVerse ScienceDirect

Surface Science Reports

journal homepage: www.elsevier.com/locate/surfrep

A review on silicene — New candidate for electronics

Abdelkader Kara [a,b,*], Hanna Enriquez [c], Ari P. Seitsonen [d], L.C. Lew Yan Voon [e], Sébastien Vizzini [f], Bernard Aufray [g], Hamid Oughaddou [b,c]

[a] Department of Physics, University of Central Florida, Orlando, FL 32816, USA
[b] Département de Physique, Université de Cergy-Pontoise, 95031 Cergy-Pontoise Cedex, France
[c] Institut des Sciences Moléculaires d'Orsay, ISMO-CNRS, Bât. 210, Université Paris-Sud, 91405 Orsay, France
[d] Physikalisch-Chemisches Institut der Universität Zürich, Winterthurerstrasse 190, CH-8057 Zürich, Switzerland
[e] Department of Physics, Wright State University, Dayton, OH 45435, USA
[f] CNRS, IM2NP, Université Aix-Marseille, Faculté des Sciences et Techniques de Jérôme, F-13397 Marseille, France
[g] CINaM-UPR3118, CNRS, Campus de Luminy, Marseille Cedex 09, France

ARTICLE INFO

Article history:
Received 23 September 2011
Accepted 10 October 2011
editor: L. Dobrzynski

Keywords:
Silicene
Silicon
Honeycomb
Epitaxial growth
Metal surfaces
Electronic structure
STM

ABSTRACT

Silicene – the silicon-based counterpart of graphene – has a two dimensional structure that is responsible for the variety of potentially useful chemical and physical properties. The existence of silicene has been achieved recently owing to experiments involving epitaxial growth of silicon as stripes on Ag(001), ribbons on Ag(110), and sheets on Ag(111). The nano-ribbons observed on Ag(110) were found – by both high definition experimental scanning tunneling microscopy images and density functional theory calculations – to consist of an arched honeycomb structure. Angle resolved photo-emission experiments on these silicene nano-ribbons on Ag(110), along the direction of the ribbons, showed a band structure which is analogous to the Dirac cones of graphene. Unlike silicon surfaces, which are highly reactive to oxygen, the silicene nano-ribbons were found to be resistant to oxygen reactivity.

On the theoretical side, recent extensive efforts have been deployed to understand the properties of standalone silicene sheets and nano-ribbons using both tight-binding and density functional theory calculations. Unlike graphene it is demonstrated that silicene sheets are stable only if a small buckling (0.44 Å) is present. The electronic properties of silicene nano-ribbons and silicene sheets were found to resemble those of graphene.

Although this is a fairly new avenue, the already obtained outcome from these important first steps in understanding silicene showed promising features that could give a new future to silicon in the electronics industry, thus opening a promising route toward wide-range applications. In this review, we plan to introduce silicene by presenting the available experimental and theoretical studies performed to date, and suggest future directions to be explored to make the synthesis of silicene a viable one.

Contents

1. Introduction 2
2. Surface alloys: semiconductor on metal surfaces 2
   2.1. Systems with tendency to order (formation of surface alloys) 3
   2.2. Systems with tendency to phase separation 4
      2.2.1. Ge/Ag(100) 5
      2.2.2. Ge/Ag(110) 6
      2.2.3. Ge/Ag(111) 6
3. Experimental investigations of silicene on silver surfaces 7
   3.1. Silicene on Ag (100) 7
   3.2. Silicene on Ag(110) 7
   3.3. Silicene on Ag(111) 11

* Corresponding author at: Department of Physics, University of Central Florida, Orlando, FL 32816, USA. Tel.: +1 407 823 1527.
E-mail address: akara@mail.ucf.edu (A. Kara).

0167-5729/$ – see front matter © 2011 Elsevier B.V. All rights reserved.
doi:10.1016/j.surfrep.2011.10.001

4. Theoretical investigations of silicene 11
4.1. Tight-binding (TB) studies of silicene 11
4.1.1. Tight-binding theory 11
4.1.2. Bulk and nanostructured silicon 11
4.1.3. Tight-binding results for graphene and carbon nanotubes 12
4.1.4. Tight-binding results for silicene and silicon nanotubes 12
4.1.5. Tight-binding results for silicane and hydrogenated silicon nanotubes 12
4.2. Density functional theory studies of silicene 13
4.2.1. "Bulk" silicene 13
4.2.2. Adsorption of hydrogen on silicene 14
4.2.3. Silicene nanoribbons 15
4.2.4. Further studies on bulk silicene 15
4.2.5. DFT investigations of adsorbed silicene on silver surfaces 16
5. Conclusion 16
Acknowledgments 16
References 17

1. Introduction

A new crystalline silicon form the so called "silicene" – the silicon-based counterpart of graphene – moved up from theoretical predictions to experimental observations in just a few years. In this review we will discuss the present status of the experimental and theoretical studies on silicene.

Before we move on to the case of silicene, we very briefly bring in the case of graphene, which has attracted a worldwide attraction. There are several carbon structures among which the well-known are graphite and diamond. A stack of planar hexagonal structure composes the former and is very popular nowadays because it has been used to extract graphene sheet [1]. Graphene is only one-atom thick layer of sp^2-bonded carbon in a honeycomb crystal structure [2] and is probably the most investigated system in materials science during the last decade. It presents striking properties, which lead to potentially novel routes for many applications [2–4].

Silicon atoms, however, have similar electronic configurations as those of carbon. In general, the explanation of why carbon makes honeycomb structures and not silicon stems from the fact that the sp^2 hybridization is more stable than sp^3 hybridization for carbon but for silicon the situation is the reverse one [5]. It is hence energetically not favorable to form spontaneously silicene from silicon atoms.

Very recently, new silicon based structures have been discovered such as single and multi-walls nanotubes (NTs), which open the door to imagine that graphene-like silicon structures could be obtained using catalysts such as surfaces.

Since the discovery of graphene, theoretical studies using *ab-initio* level calculations [6,7] attempted to establish theoretical similarities between carbon NTs and hypothetical silicon NTs, such as band structure and density of states. Fagan et al. predicted that the electronic properties of single-wall silicon NTs are very similar to the equivalent carbon NTs [6]. From the experimental point of view, silicon tubular structures and NTs have been synthesized by different process [8–10], which raised the question of the existence of other crystalline forms of silicon, different from the well-known diamond structure.

Two-dimensional silicon nanostructures were probably first fabricated by solution-based methods. Thus, Nakano et al. made silicon sheets by chemical exfoliation of $CaSi_2$ [11]. Nevertheless, they were Mg-doped, had silicon bonded to oxygen, and were proposed to be ⟨110⟩ oriented. Tunneling electron microscopy (TEM) and atomic force microscopy (AFM) images revealed a hexagonal structure with atomic separations of about 0.41 nm. In order to obtain oxygen-free nanosheets, Okamoto et al. [12,13] performed exfoliation of layered polysilane by reaction with n-decylamine, leading to Si(111) planes with amines covalently bonded. In their study, Okamoto et al. reported that these nanosheets are "free-standing" with a thickness less than 2 nm. Time-resolved photoluminescence measurements with emission at 435 nm indicate that these nanosheets belong to the class of direct gap materials. Synthesis of silicon nanowires by chemical etching has also been reported as well [14].

In 2007, Guzmán-Verri and Lew Yan Voon developed a tight-binding (TB) Hamiltonian that takes into account the electronic properties of Si NTs and silicene [15]. These results show that silicene is semi-metallic. Subsequently, two other theoretical studies [16,17], using density functional theory (DFT), have shown that a silicon quasi-two dimensional structure is stable. Several others then followed these studies, which will be discussed in details in the present review. On the other hand, recent experimental studies explored the epitaxial adsorption of silicon on silver surfaces resulting in an evidence of the possible formation of silicene nano-ribbons (NRs) and sheets [18–25]. This has been supported by *ab initio* calculations for silicene NRs on Ag(110) [26].

Since surface alloying is a key mechanism to the formation of silicene by epitaxial growth on metal surfaces, this review will contain a description of surface alloying as relevant to the case at hand (Section 2). The experimental investigations of silicene on silver surfaces will be detailed in Section 3, while Section 4 will be devoted to the theoretical studies of silicene. Finally, our conclusions and future plans for silicene will be presented in Section 5.

2. Surface alloys: semiconductor on metal surfaces

Temperature dependence of metallic thin films deposited on metallic substrates has been the subject of many investigations in relation to possible technological applications. Indeed, the formation of surface alloys, which appear during the dissolution process of a thin film, can present new chemical and physical properties with regard to their small thickness (typically a few atomic layers). The composition of these surface alloys is closely related to both chemical interactions between elements (deposit and substrate) and a surface segregation tendency [27]; for a review, see for instance Refs. [28–30]. Most modern theories [31,32,28] describe the surface segregation phenomenon in metallic alloys as resulting from three main driving forces: (i) relative surface stress of pure elements; (ii) chemical interactions; and (iii) size mismatch. According to these models, the segregation phenomenon can in some cases appear as a precursor of the bulk phase transformations. Thus, surface segregation can lead to the formation at the surface of a pure plane of solute for systems showing a tendency to phase separation, and a two-dimensional ordered surface alloy for systems presenting a tendency to order. This has been experimentally observed for two model metallic systems: Ag/Cu(111) (phase separating system) [33,34] and

Sb/Cu(111) (ordering system) [35,36]. This segregation behavior induces different dissolution kinetics in both cases in order to preserve a local equilibrium in the surface selvedge. Indeed, the dissolution kinetics at 450 °C of one monolayer of silver deposited on Cu(111) are slower than those expected (due to the tendency of silver to segregate), while obeying a square root of time dependence law which is the signature of a surface transition from a quasi-pure silver layer to a quasi-pure copper layer [33,34]. On the contrary, at the same temperature, the dissolution kinetics of one monolayer of antimony deposited on Cu(111) are not slowed down at the beginning but are later blocked when the surface concentration corresponds to a surface alloy Cu_2Sb forming a $(\sqrt{3}\times\sqrt{3})R30^\circ$ surface superstructure [37]. Both kinetic behaviors on Cu(111) have been theoretically simulated using the kinetics tight-binding Ising model (KTBIM) [38,39] either in a mean field approximation or/and within Monte Carlo simulations [40], in order to take into account only the three main driving forces for segregation that are previously mentioned.

Metal on metal systems show small crystallographic structural differences; therefore chemical interactions are sufficient to account for the previous trends. However, this should not be the case for semiconductor on metal systems because they present drastically different crystallographic structures, related to the drastic difference in chemical bonding (covalent versus metallic). In such a picture one can expect stronger structural effects such us alloying, either as an ordered or amorphous super-structure.

The growth of noble metals on semiconductor surfaces has been the subject of a large number of studies in the recent years [41–46]. These studies have been motivated for understanding the interface properties such as the Schottky-barrier formation [47,48]. Besides the large variety of metal/semiconductor interface studies, the investigation of the reverse semiconductor-on-metal interface is also important since inequivalency can be expected between the two materials. Indeed, it is known [49] that the variation of the deposition sequence may not only affect the interface morphology, but also the chemistry of the interface inducing the formation of new compounds.

Surprisingly, they are very few studies devoted to the deposition of semiconductors on metallic surfaces. The first studied systems have tendency toward ordering i.e. forming ordered compounds such as silicides or germanides [41,50–52]. For such a case, we expect formation of surface alloys; however, systems with tendency toward phase separation are expected to form a stable semiconducting atomic layer on the metal surface.

2.1. Systems with tendency to order (formation of surface alloys)

The Si/Cu(110) was the first prototype of semiconductor on metallic surfaces [52–54]. The phase diagram of this system presents a tendency to form an alloy. This system has been analyzed with Scanning Tunneling Microscopy (STM), Low Energy Electron Diffraction (LEED), and Photo-Electron Spectroscopy (PES).

Room temperature (RT) deposition of 0.5 monolayer (ML) of silicon on a Cu(110) surface leads to the formation of a $c(2\times2)$ superstructure [52–54]. For silicon coverage of 0.1 ML, structured islands are observed on the surface aligned along the ⟨-112⟩ direction (Fig. 1). These islands grow and coalesce upon increasing silicon coverage, resulting in the formation of extended alloy areas. Complete $c(2\times2)$ surface alloy terraces are observed for silicon coverage of 0.5 ML (Fig. 2).

The structural study by quantitative analysis of LEED intensities confirms the formation of a two-dimensional alloy with Si atoms in substitutional Cu sites (Fig. 3) [53]. High-resolution synchrotron-radiation photoemission spectroscopy (HR-PES) has been also used to investigate the surface alloy superstructure and the STM images have been correlated to photoelectron-diffraction [54]. This study has evidenced the formation of surface alloys.

Beyond the 0.5 ML silicon coverage, the LEED pattern evolves toward a (2×2) structure [50]. The STM images show a linear atomic Si chains on top of the surface alloy layer (Fig. 4).

Annealing the (2×2) structure at 250 °C, leads to a quasi-(3×4) structure forming similar chains exhibiting a different periodicity (Fig. 5).

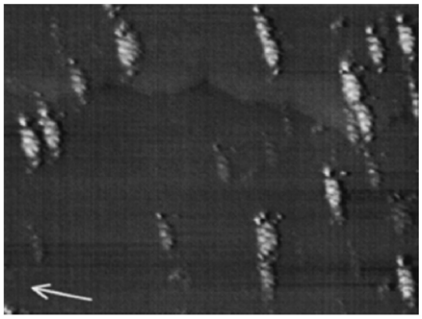

Fig. 1. 160 × 160 nm² STM image of the Cu(110) surface after deposition of less than 0.1 Si ML at RT. A step on Cu(110) is seen at the upper part of the image. Alloy clusters are aligned along ⟨-112⟩ surface direction. The arrow indicates the ⟨-110⟩ surface direction (by courtesy of J.A. Martín-Gago [50]).

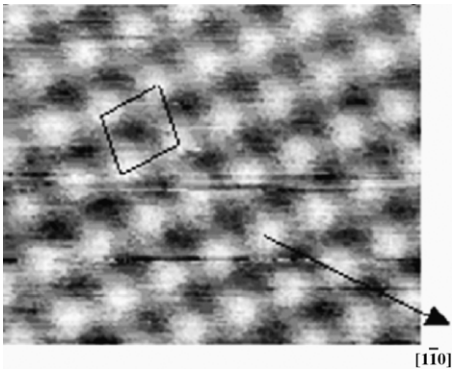

Fig. 2. STM image showing atomic resolution obtained for 0.5 Si ML coverage. The $c(2\times2)$ unit cell is indicated (courtesy of J.A. Martín-Gago [50]).

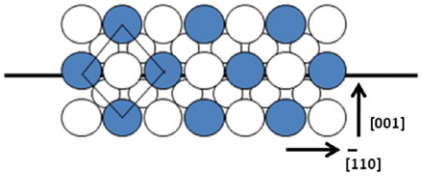

(a) Top view.

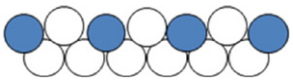

(b) Side view.

Fig. 3. Structural model for the $c(2\times2)$ surface alloy: (a) top view, and (b) side view. The $c(2\times2)$ unit cell is shown in the figure. Filled and empty circles represent Si and Cu atoms, respectively (courtesy of J.A. Martín-Gago [50]).

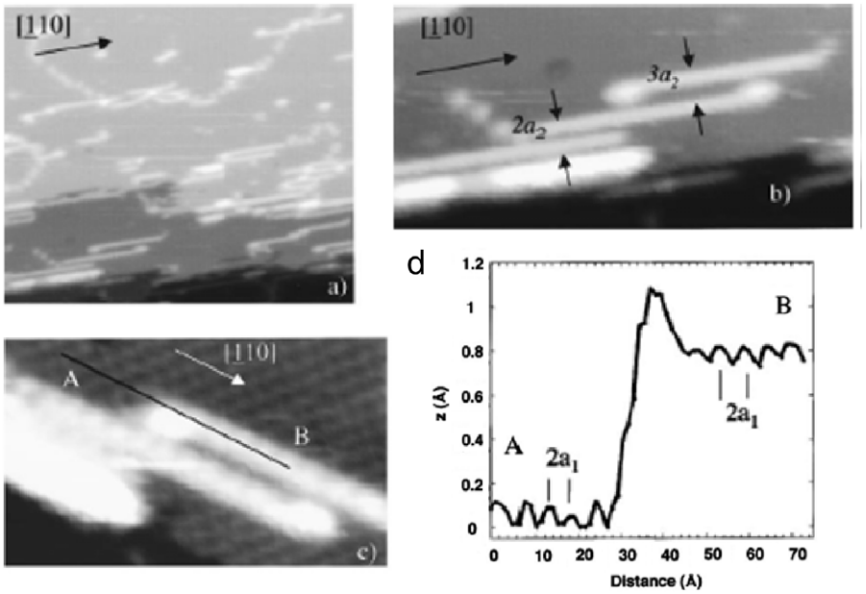

Fig. 4. STM image of the surface after deposition of 0.55 Si ML on Cu(110). (a) A general view of the surface (33×28 nm^2), (b) Si chains on c (2×2) surface alloy (15×7.5 nm^2), (c) individual Si chains (10×5 nm^2), (d) Profile along the line represented in (c) (courtesy of J.A. Martín-Gago [50]).

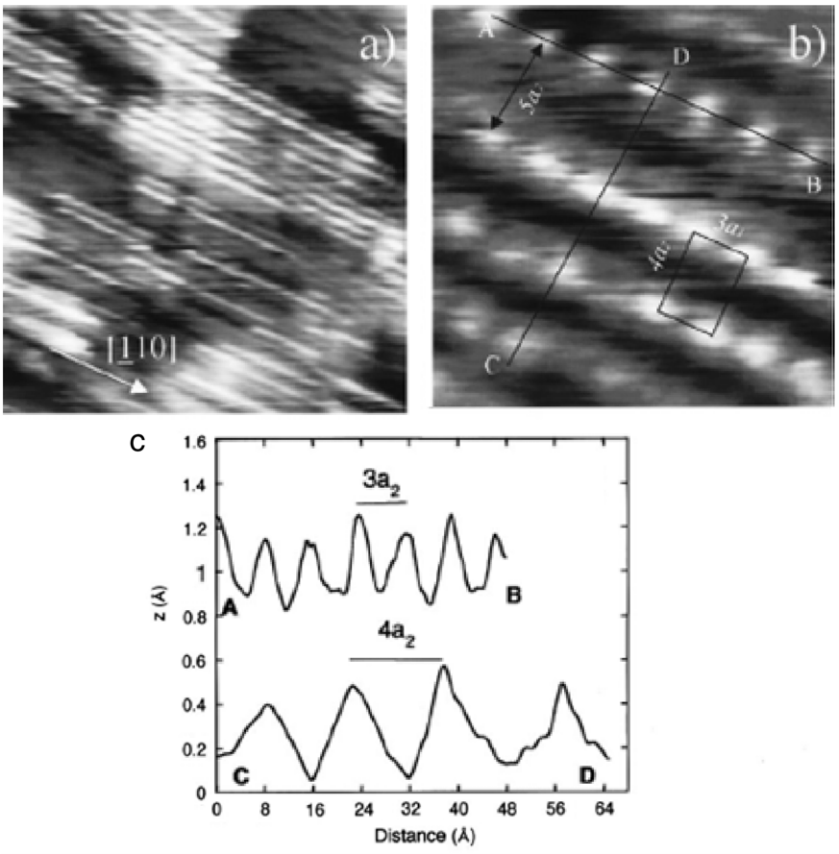

Fig. 5. STM images of the surface after deposition of 0.8 ML silicon on Cu(110) and posterior annealing at 250 °C. (a) overview of the surface (48×48 nm^2), (b) detail of the linear chains (6.2×6.2 nm^2), (c) profiles along the indicated directions of (b) (courtesy of J.A. Martín-Gago [50]).

2.2. Systems with tendency to phase separation

For systems presenting tendency toward phase separation, each atom maximizes its number of neighbors in a close-packed structure, in contrast with interactions in semiconductor that favor the formation of oriented bonds, often at the expense of the compact packing compacity. This often may leads to a new type of surface alloy, as we shall see.

The prototype system for this case is Ge/Ag, which presents a strong tendency toward phase separation as shown by the bulk phase diagram [55,56] and a large germanium surface segregation. The thermal behavior of Ge thin film on silver was studied by Auger

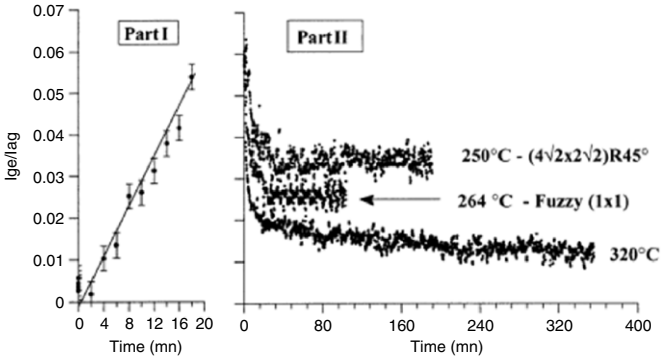

Fig. 6. Part I illustrates an example of the deposition of about one monolayer of germanium and Part II is the dissolution kinetics in the bulk recorded for different temperatures just after deposition.

Electron Spectroscopy (AES), LEED, STM, Surface X-ray Diffraction (SXRD) as well as PES [57–65].

2.2.1. Ge/Ag(100)

The growth of Ge on Ag(100) at RT was found to be close to the layer by layer mode [57,58]. For 0.5 Ge ML, The LEED shows a p($4\sqrt{2} \times 2\sqrt{2}$)R45° superstructure, which becomes more and more intense as the germanium coverage increases.

The thermal behavior of Ge on Ag(100) was studied by following the dissolution kinetic of 1 ML of Ge on Ag(100). The variations of Ag and Ge Auger peak-to-peak intensity ratio (I_{Ge}/I_{Ag}) versus time are displayed in Fig. 6.

Both kinetics that are recorded at 250 and 264 °C, show that at the beginning of annealing, a rapid dissolution occurs followed by a blocking of this dissolution on a plateau whose level depends on temperature. At 320 °C, a rapid dissolution at the beginning of the kinetics is observed followed by a slower one up to a quasi-complete dissolution. The LEED observations carried out at room temperature at the end of each run exhibit: (i) a sharp and well defined $p(4\sqrt{2} \times 2\sqrt{2})$R45° LEED pattern after dissolution at 250 °C, (ii) a fuzzy (1 × 1) LEED pattern after dissolution at 264 °C, (iii) a sharp (1 × 1) LEED pattern after dissolution at 320 °C in good agreement with the quasi complete dissolution observed on the kinetics.

The kinetic behavior for Ge on Ag(100) is closer to those obtained for systems with a tendency to order (Sb/Cu) [35,36] than to those obtained for systems with a tendency toward phase separation (Ag/Cu) [33,34]. In addition, the complete monolayer of germanium seems to increase the silver surface free energy since the effect is reversed when comparing surface energies of both pure elements (Ge = 0.88 J m^{-2} and Ag = 1.25 J m^{-2} [50]). This special behavior was correlated to the covalent nature of germanium for which a (100) fcc type two-dimensional layer is highly unstable. The germanium prefers an atomic structure closer to its diamond-like character, which generates a strong surface stress (due to the structural incoherence between silver and germanium) and increase the total surface free energy leading to the fast dissolution of the (100) fcc germanium layer. From this point of view, such behavior suggests the possibility to obtain a new class of surface alloys driven by structural coherence effects when substrate and deposited elements present very different types of chemical bonding.

Fig. 7a shows the STM image corresponding to the p(2v2 × 4v2)R45° superstructure [58]. It shows wavy rows of white spots in one direction that we assigned to small clusters of Ge. These clusters correspond to four Ge atoms (tetramers) as it can be seen in Fig. 7b once the atomic resolution has been achieved. Previous SXRD study [58] has reported the formation of Ge tetramers located in adatom positions on the Ag surface. Three of the Ge atoms are in the hollow sites and the fourth one is near a bridge position.

The dissolution at 250 °C gives rise to the same structure as in Fig. 7a indicating the stability of Ge tetramers. However, after a few minutes of annealing at 260 °C, the appearance of a set of black squares indicates dissolution, which is attributed to "Ge tetramer vacancies". These vacancies are not randomly distributed on the surface but are locally ordered on two or three periods (Fig. 8a) [59]. The two ordered structures of "vacancies" (L1 and L2) observed after this annealing are shown on Fig. 8b.

Fig. 9a shows an STM image (50 nm × 50 nm) of the surface recorded after a further 20 min annealing of the sample maintained at 260 °C. In this STM image one can see that the dissolution effect is more important. One observes not only the same square structure (L1) as in Fig. 8b but also a new one (labeled L3), with a "zigzag-like" shape. A magnification of a part of these domains is reported in Fig. 9b revealing the details of this new arrangement of "tetramer vacancies".

The first interesting point of this set of results is that, as expected from all previous kinetics studies recalled above, the existence of a plateau on a dissolution kinetics recorded by AES [57] corresponds to a specific surface structure. In this case, the absence of LEED pattern at the end of the kinetics was due to the size domains of these arrangements of "tetramer vacancies" which are too small to give rise to a strong coherent signal. The second and striking point is the quasi absence of trimers, dimers and monomers (isolated atom) of Ge during the dissolution process. The Ge dissolution proceeds by successive disappearance of Ge tetramers confirming the large stability of the latter on the Ag(001) surface.

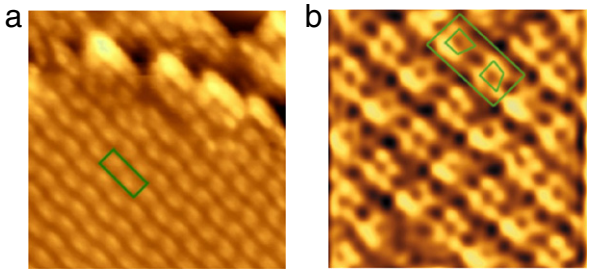

Fig. 7. (a) Filled-state STM image of a 10 nm × 10 nm area surface after deposition of 0.5 ML of germanium at room temperature (the unit cell is shown as a rectangle), (b) Atomically resolved STM images.

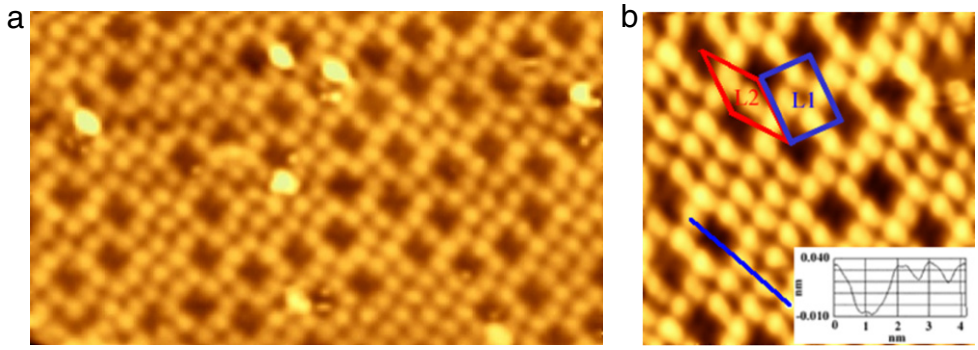

Fig. 8. (a) Filled-state STM images of 20 nm × 20 nm area of the Ag(001) surface recorded at room temperature after a short annealing of the sample at 260 °C for a few minutes. (b) The same filled-state STM image for a 10 nm × 10 nm area.

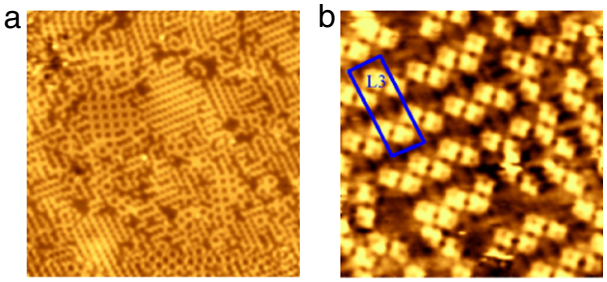

Fig. 9. (a) STM images (50 nm × 50 nm) of the surface recorded after a further annealing of the sample for 20 min maintained at 260 °C. (b) Magnification of the figure to reveal the details.

2.2.2. Ge/Ag(110)

The adsorption of germanium on Ag(110) has been also investigated by STM, LEED as well as SXRD [60]. After deposition of 0.5 Ge ML coverage, the LEED pattern revealed a $c(4 \times 2)$ superstructure. The STM images corresponding to the $c(4 \times 2)$ superstructure at the atomic resolution show two Ge tetramers in the surface unit cell (rectangle) (Fig. 10).

Based on the STM images and SXRD measurements, an atomic model of the surface structure with Ge atoms forming tetramer nano-clusters that are perfectly assembled in a two-dimensional array over the silver top layer was proposed [60].

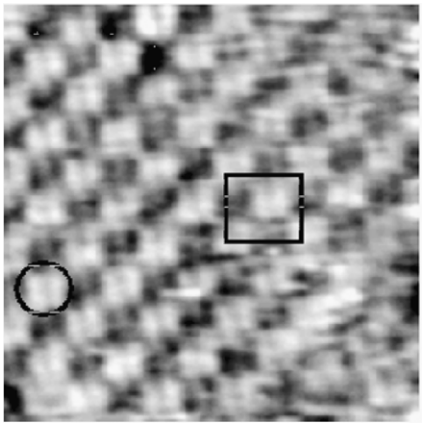

Fig. 10. Empty state STM image (8 × 8 nm^2, $V = 40$ mV, $I = 1.76$ nA) showing the $c(4 \times 2)$ superstructure at atomic resolution with two tetramers in the surface unit cell (rectangle). The tetramer (circle) is clearly noticeable.

2.2.3. Ge/Ag(111)

On the (111) surface, the LEED pattern shows a $(\sqrt{3} \times \sqrt{3})R30°$ after deposition of 1/3 ML of Ge [36,37]. This superstructure becomes fuzzy beyond this coverage and a new $c(\sqrt{3} \times 7)$ LEED pattern appears and become sharper at 1 ML of Ge coverage. Fig. 11 shows an atomically resolved STM image of the surface with 1/3 ML of Ge deposited at room temperature displaying a sharp $(\sqrt{3} \times \sqrt{3})R30°$ LEED pattern. The surface observed by STM appears identical to a pristine Ag(111) surface, exhibiting no chemical contrast (as confirmed in different places on the surface for both positive and negative biases between +0.5 and −0.5 V). The vertical corrugation is found to be about 0.3 Å, whereas the lateral distance between two atoms is (3.1 ± 0.2) Å, which is close to the expected Ag–Ag distance in the (111) plane. This distance is definitely different from the parameter (∼ 5 Å) of the $(\sqrt{3} \times \sqrt{3})R30°$ superstructure. No effect of the sign of the bias voltage was possible, which revealed the metallic character of the surface. Beyond this coverage, a $c(\sqrt{3} \times 7)$ superstructure appeared and became sharper at 1 ML of deposition.

The $c(\sqrt{3} \times 7)$ superstructure is built up by self-assembled tetramer Ge nanodots: four tetramers per $c(\sqrt{3} \times 7)$ unit cell (sixteen Ge atoms in the unit cell) (Fig. 12) [64]. The four Ge atoms within these nanodots are not close-packed but form a rather open tetramer, which seems, at first glance, quite similar to what has been observed on the Ag(001) and Ag(110) surfaces [58,60].

At variance with Ag(001) and Ag(110), for the $(\sqrt{3} \times \sqrt{3})R30°$ superstructure, the germanium atoms are incorporated in the first silver layer forming an ordered Ag_2Ge surface alloy [61]. This behavior on the (111) face is quite surprising since the chemical tendency of the system is to form homo-atomic bonds, as the bulk phase diagram displays a large miscibility gap. These very different behaviors could be related to the initial surface structures or/and to different germanium interactions with the metallic substrate. Such behavior was also observed in the case of metallic system, Pb/Ag system, which has tendency to phase separation [66–68]. The Ge 3d core levels of the $(\sqrt{3} \times \sqrt{3})R30°$ was analyzed by PES [61]. Its metallic state is well corroborated by the set of spectra shown in Fig. 13 recorded during the first step of the growth.

For each spectrum of the Fig. 16, the binding energy is referenced to the Fermi level. Using a Doniach–Sunjic line shape, the Ge 3d spectra have been fitted with two components (S1) and (S2) at 28.80 and 29.07 eV binding energies, respectively (in the whole coverage range). The (S1) component of the spectrum is attributed to the $(\sqrt{3} \times \sqrt{3})R30°$ superstructure. The (S2) component, which is weak at low coverage and increases markedly beyond 1/3 ML, is assigned to the growing second superstructure $c(\sqrt{3} \times 7)$, at the expense of the $(\sqrt{3} \times \sqrt{3})R30°$, which begins to disappear.

The comparison of the surface structures obtained on the three faces of low indices i.e. (001), (110) and (111), indicates the significant role played by both Ge–Ge and Ge–Ag interactions (on the surface structures) obtained after deposition. More generally, the open structure adopted by the germanium atoms

reveals the delicate balance between metallic and semiconductor-like interactions. On each face orientation it results from the competition between the Ge–Ge interactions, which tend to favor the most compact tetramers, while the Ge–Ag interactions can be strong enough at the surface to favor the formation of a surface alloy.

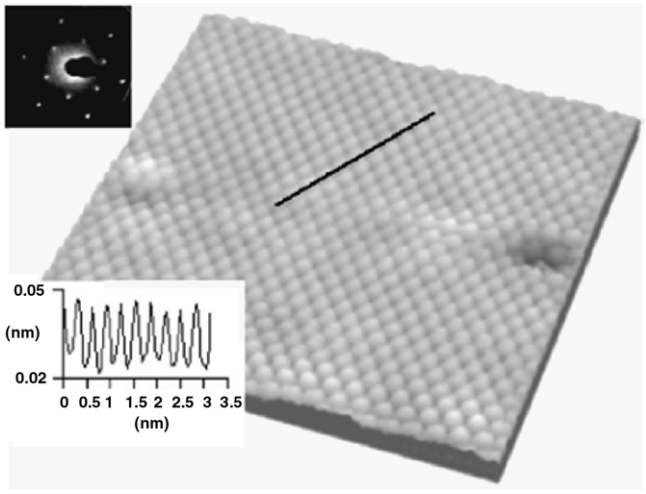

Fig. 11. ($\sqrt{3} \times \sqrt{3}$)R30° LEED pattern ($E_p = 52$ eV) left-upper corner. Filled-state STM image (6.4 nm × 6.4 nm, $V = -50$ mV, $I = 2.0$ nA). A line scan along the [110] direction gives the corrugation shown in the lower-left corner.

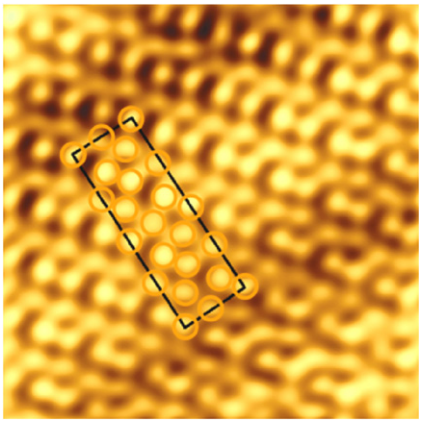

Fig. 12. Filled-state STM images (3 × 3 nm^2, $V = -0.005$ V, $I = 5$ nA) showing the local arrangement within the $c(\sqrt{3} \times 7)$ superstructure unit cell.

3. Experimental investigations of silicene on silver surfaces

The Si/Ag system has a marked tendency toward phase separation [55,56] with very low solubility of Si in bulk Ag at the difference of the large solubility of Ge in Ag. Unlike Ge/Ag system, the formation of Si structures is expected to take place only on top of Ag surface without any Si diffusion.

3.1. Silicene on Ag (100)

On the Ag(100) surface, the growth at RT was found to be layer-by-layer without formation of any ordered structure [69]. However, annealing at 230 °C or during the growth at the same temperature, two ordered surface structures were observed. The first structure was obtained from the first stages of growth up to one monolayer, and corresponds to a p(3 × 3) superstructure for

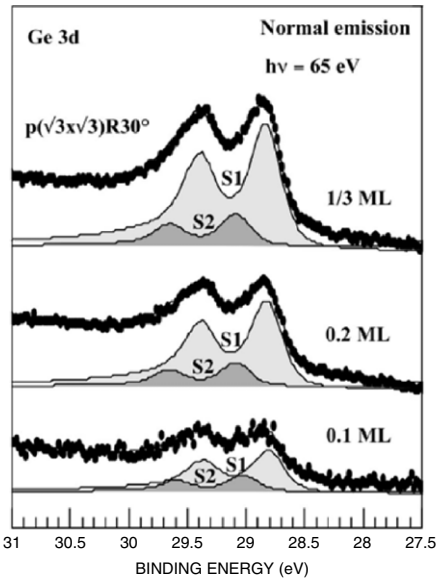

Fig. 13. Ge 3d core-level spectra recorded at normal emission at a photon energy of 65 eV during the growth.

which a precise atomic model was established on the basis of SXRD and STM measurements [18]. The unit cell of this superstructure contains one silicon tetramer composed by two tilted Si dimers. STM images showed the self-organization of these tetramers in 1D stripes oriented along the [110] or the [-110] directions (Fig. 14).

Beyond the one ML silicon coverage, a complex superstructure was shown to take place with no discernible long-range order symmetry as indicated by LEED [18]. The STM topography revealed the local coexistence of two superstructures, the previous $p(3 \times 3)$ together with new silicon stripes made of two joined chains of regular hexagons oriented along [110] or [-110] directions (Fig. 15), and forming a p(7 × 4) local superstructure. These stripes have a width of $7a_{Ag}$ (surface Ag parameter), and the chains of hexagons present a $4a_{Ag}$ periodicity along the stripes [18].

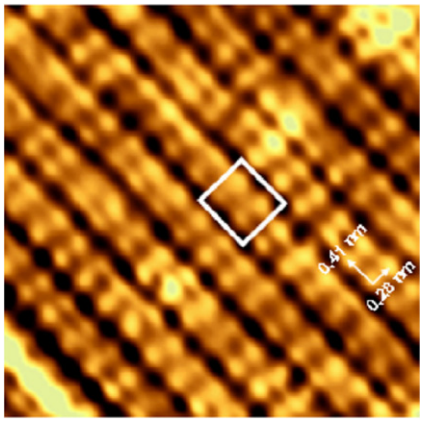

Fig. 14. Filled-state STM image (6.4 × 6.1 nm^2, $V = -1.02$ V, $I = 1.14$ nA) showing the atomic resolution of the $p(3 \times 3)$ structure. The unit cell is indicated by a square.

3.2. Silicene on Ag(110)

The first silicon structures observed on a Ag(110) substrate were described as silicon nanowires (NWs) obtained by Si deposition under UHV conditions in the sub-monolayer range [19]. The STM measurements revealed several characteristics of these NWs (Fig. 16), namely the precise crystallographic orientation

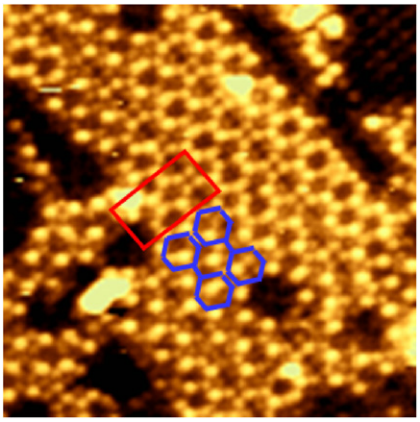

Fig. 15. Filled state STM image (6.4×6.4 nm^2 $V = -1$ V, $I = 1$ nA) of the "complex structure". The local $p(7 \times 4)$ unit cell is indicated. The pattern of two joined chains of hexagons is drawn in blue.

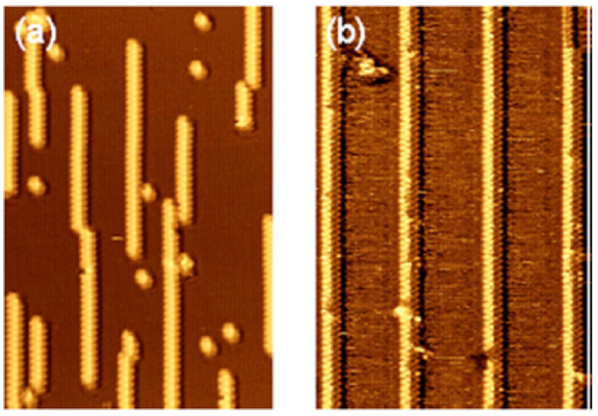

Fig. 17. (24.3×36.1 nm^2) topographic STM images of a low coverage of Si deposited at room temperature on a Ag(110) surface. (a) Before annealing ($V = -1.7$ V, $I = 1.1$ nA). (b) After annealing at 230 °C ($V = -0.4$ V, $I = 0.7$ nA).

(parallel to [-110] Ag direction), a height of 0,2 nm, and a well-defined width of 1,6 nm equal to $4a_{Ag[100]}$, i.e. four times the lattice parameter of the substrate in the perpendicular [100] direction. Moreover, a periodicity of $2a_{Ag[1\bar{1}0]}$ was observed along the NWs in the STM topography, which was corroborated by half-order diffraction spots in the [1-10] direction of the LEED pattern [19].

While the width of the NWs is precisely defined, the length obtained after RT silicon deposition is very disparate (1.5–30 nm), including both Si nanodots and NWs [19] (see Fig. 16a). However, annealing at 230 °C induced a significant elongation of the NWs well beyond 100 nm, while keeping the same 1.6 nm width as shown in Fig. 17 [19]. Furthermore, for long annealing times, the nanodots shown in Fig. 17a disappear while being incorporated to the Si NWs (Fig. 17b). Therefore, the NWs formation is the result of a 1D diffusion process, allowing the self-assembly of nanodots along [-110] direction and not in the perpendicular [100] direction.

The strong anisotropy of Si nanodots self-assembly on Ag (110) was also confirmed by a study of Si growth on a silver substrate kept at 200 °C. In this case, at one Si ML coverage, a grating of one-dimensional NWs was evidenced, presenting a 5×2 periodicity, as shown both in the LEED pattern and in the STM images (Fig. 18) [70]. The silver substrate is fully covered by Si NWs exhibiting the same width of $4a_{Ag[100]}$ with a regular spacing of $5a_{Ag[100]} \approx 2.05$ nm instead of the random spacing (1.5–15 nm) previously observed. The ($\times 2$) periodicity along the [-110] direction was observed, as in the case of isolated NWs.

In the Si NWs, it is clear that the rounded protrusions composing the row with a $2a_{Ag[1\bar{1}0]}$ periodicity were too large to represent individual atoms [19,70]. A key point in understanding the structure of the nanowires was the observation of a clear asymmetry in the height profile measured perpendicular to the NWs as seen in Fig. 16c [19]. This asymmetry was shown to be related to a misalignment between the right and left sides of the protrusions in a wire, corresponding to a glide of one $a_{Ag[1\bar{1}0]}$ lattice parameter that is clearly visible in the 3D view of Fig. 19 [71,70,26]. Moreover, the height profile asymmetry was extended to the Ag substrate close to the NWs, since a dip was noticeable on one side of the NWs [71,70].

The internal structure of a Si NW as well as its bonding to the substrate has been elucidated recently [23,26]. With even higher

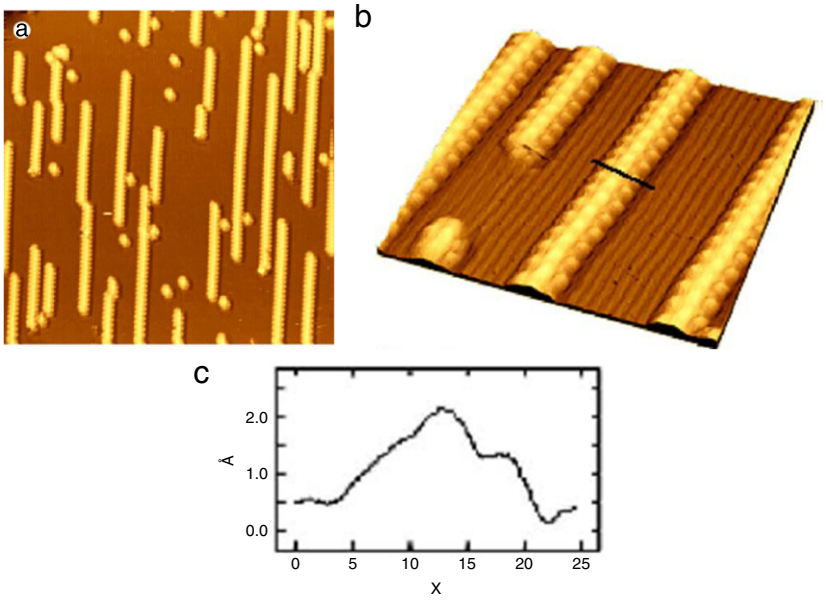

Fig. 16. Topographic images ($V = -1.7$ V and $I = 1.1$ nA) of the 0.25 ML of silicon deposited on Ag(110) at room temperature showing Si NWs: (a) 42×42 nm^2, (b) 12.1×12.1 nm^2. (c) Line profile along the black line drawn in (b).

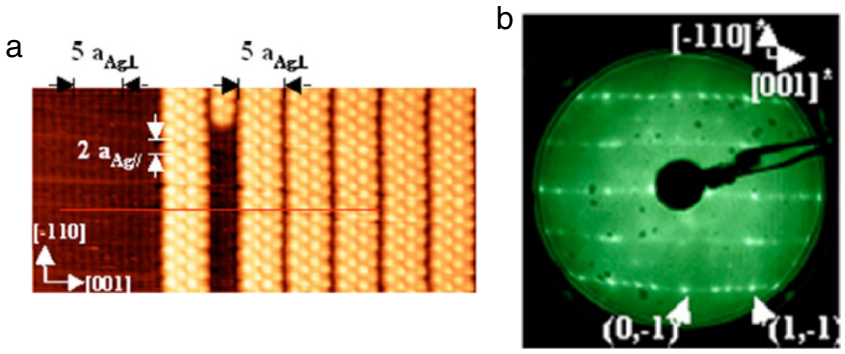

Fig. 18. (a) (17.4 × 8 nm^2) topographic STM image of the 5 × 2 silicon NWs reconstruction on Ag(110) ($V = -1.7$ V, $I = 0.3$ nA). (b) 5 × 2 LEED pattern at 68 eV primary energy.

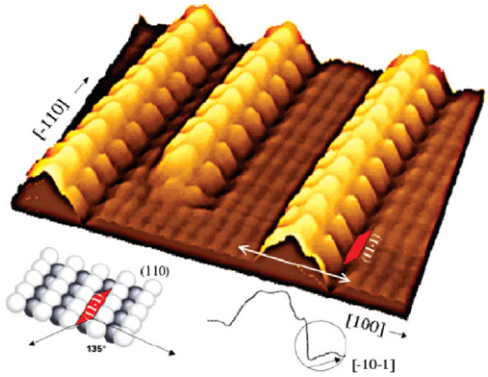

Fig. 19. 3D view of a 10.2 × 10.2 nm^2 filled-states STM image: dip asymmetry at right-side. High resolution STM topography images of isolated NWs show a structural signature of this transverse asymmetry, mainly a structure formed by a square and a parallelogram side-by-side, having a common side of 2a$Ag_{[1\bar{1}0]}$ with a glide of one a$Ag_{[1\bar{1}0]}$ along [-110] for the other parallelogram side (Fig. 20) [21].

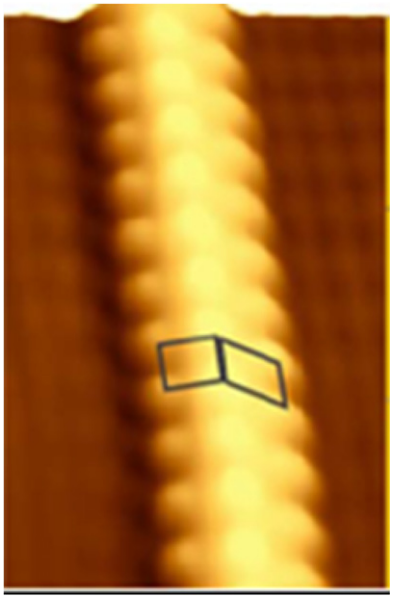

Fig. 20. Square joined to a parallelogram drawn on the STM image of a Si stripe.

resolution, STM experiments allowed to resolve silicon hexagons in honeycomb arrangement inside the NW (Fig. 21) [23]. Along the direction 30° away from the [-110] Ag direction, one counts four Si hexagons in a NW that, at this point, has been named "silicene nanoribbons (NRs)".

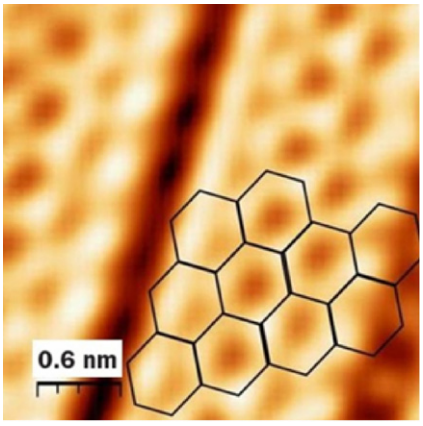

Fig. 21. High resolution filled state STM image revealing honeycomb arrangement.

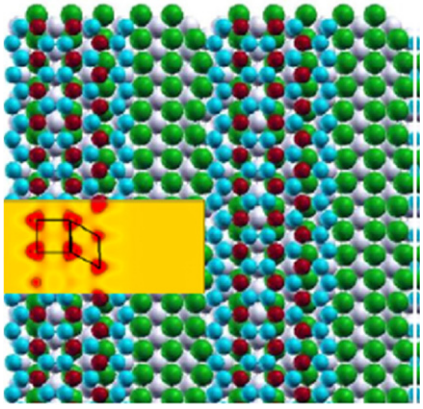

Fig. 22. Top view of Si NRs structure calculated on Ag(110): silicon (red/blue) forming hexagons on top of the surface Ag atoms (green). (For interpretation of the references to colour in this figure legend, the reader is referred to the web version of this article.)

The finding of a hexagonal Si structure on the rectangular Ag (110) substrate gives a possible explanation of the asymmetry of the Si NW. The rather complex structure of the latter has been elucidated with the help of *ab initio* calculations based on DFT [26]. The optimization of a Si NR configuration involving 30 Si atoms on a five layers thick (4 × 6) Ag(110) supercell, showed that the Si atoms tend to form a honeycomb structure on the Ag substrate. Most important, the Si honeycomb structure presented a noticeable buckling after full relaxation of the system. This buckling was found to be responsible for the asymmetric corrugation in the charge density profile, as well as for the imaging

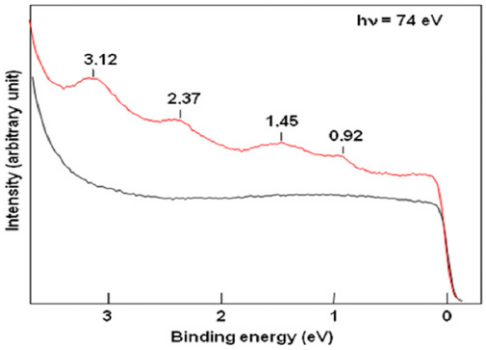

Fig. 23. Normal incidence valence band angle integrated spectra measured at $h\nu = 79$ eV for the initial pristine Ag(110) surface (bottom curve) and after a 0.25 ML of silicon has been deposited at room temperature (top curve).

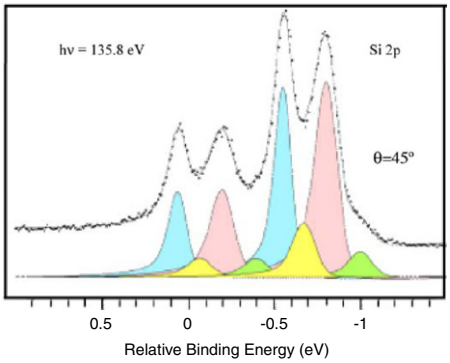

Fig. 24. The Si2p core level spectrum and its de-convolution (bottom curves). The spectrum was recorded at normal incidence and at $h\nu = 140$ eV; with an emission angle of 45°.

of the topmost atoms as square attached to parallelogram in STM images (Fig. 22) [26].

Therefore, the Si nanostructures that were initially considered as NWs on Ag(110) can be better described as NRs of silicene forming an arc with a height of roughly 0.2 nm; the bending of the nanoribbons being induced by the incommensurability with the rectangular Ag substrate. The asymmetry of the bent NRs also involves the substrate Ag rows: on one side of the ribbon, the silver atom chain displays displacements from the ideal atomic positions both in and out of the plane, whereas the chain on the other side is not affected. This corresponds to the dip previously observed only on one side of the height profile.

One consequence is the chiral coupling between NRs that is probably mediated by the Ag substrate. The observed NRs are organized in large left-handed (or right-handed) domains, estimated to be several microns per side [71]. The right (resp. left) asymmetry of the NR corresponds to a dip on the right (resp. left) side of the height profile.

The electronic properties of silicene NR grown on Ag(110) were investigated by different experimental techniques including valence band and core-level photoemission spectroscopy [19,72, 25] and scanning tunneling spectroscopy (STS) [73].

As a first indication for the metallic character of the system, the valence band measurements displayed an increase of the density of states (DOS) at the Fermi energy E_F as compared to the bare silver surface (Fig. 23) [19]. The normalized differential conductance (dI/dV)/(I/V) obtained by STS also exhibited a non-zero local density of states (LDOS) between −2 and 2 eV, as well as a monotonic increase in current with bias [73].

The Si 2p core-level spectroscopy confirmed the metallic character of the silicon NRs, since all spectra taken at various photon energies; incidence and detection angles were systematically

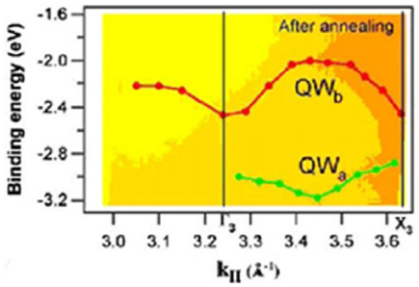

Fig. 25. Dispersion of the two quantum states measured along the ΓX direction of the second and third surface Brillouin zones for a 0.25 silicon monolayer covered Ag(110) surface after 230 °C annealing. $h\nu = 75$ eV, and with 45° incidence. Binding energies are referenced to the Fermi level.

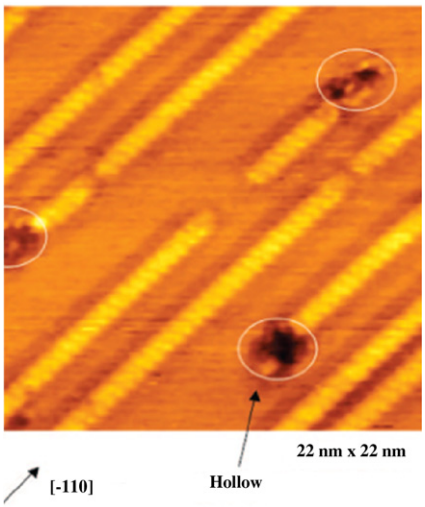

Fig. 26. (22×22 nm^2) topographic image of Si NRs on Ag(110) at 15L oxygen dose. The circles show the hollows announcing the unset of the oxidation process.

asymmetric. The Si2p spectrum was de-convoluted in two main spin–orbit split components (Fig. 24) [19,71]. The best fitting of the spectra included an asymmetry parameter of 0.09 or 0.122, which was believed to be higher than that reported for the Ag 3d on a clean silver surface [19,71]

Furthermore, the angle-integrated valence band measurements indicated the appearance of four new discrete electronic states in the proximity of E_F, at 0.92, 1.45, 2.37 and 3.12 eV binding energies. These states are clearly noticed in the measurement geometry of Fig. 23, i.e. at normal incidence and at 45° emission along the [-110] direction. A peak at −0.89 V was observed in the STS data [73], in good agreement with the 0.92 eV feature measured by photoemission. These states do not correspond to any surface state of the pristine silver. As these states do not disperse at normal emission as a function of photon energy, they were then assigned to surface states characteristics of the Si NRs. A detailed angle-resolved photoemission study of the two deepest discrete states was performed, revealing a lack of dispersion along the [100] direction, perpendicular to the ribbons, and a significant dispersion by 0,4 eV along the [-110] direction parallel to the ribbons (Fig. 25) [19].

Interestingly, no dispersion was observed along [-110] if no annealing at 230 °C is performed, i.e. for Si nanodots not yet organized in 1D structures on the Ag surface [70]. Therefore, the discrete states were rationalized as an effect of quantum confinement in at least two directions: along the normal to the surface and in the [100] direction. In the [-110] direction, the 1D dispersion measured for elongated nanoribbons indicated 1D character, whereas confinement was observed for Si nanodots.

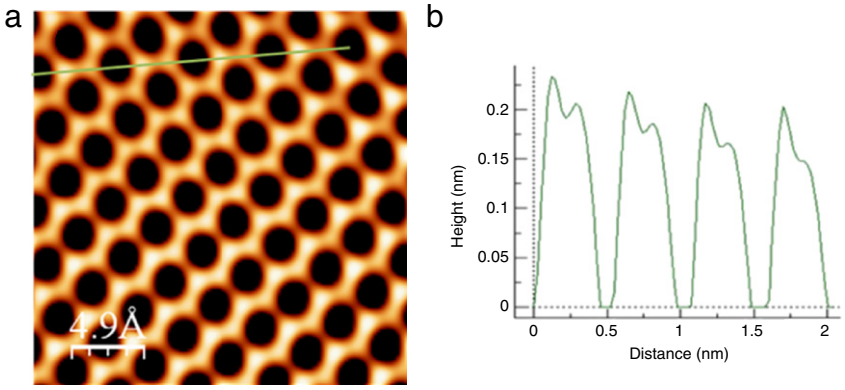

Fig. 27. (a) Filled-state atomically resolved STM image showing honeycomb structure, revealing two sublattices. (b) Line-profile joining neighboring Si atoms along the direction indicated in (a).

Hence for Si NRs on Ag (110), there is coexistence of quantum confinement and metallicity. On the contrary, it was reported that Si NWs with diameter in the 1.3–7 nm range made using lithographic patterning or by chemical synthesis are known to be semiconducting with an increase of the electronic energy gap with an increase in the quantum confinement effects [75]. This different behavior may be attributed to the silicene structure of the NRs and/or to the hybridization of the Si and Ag electronic states.

The oxidation process of the Si NR was also studied at the atomic scale both by STM and PES [22]. Exposure to molecular oxygen of the surface was performed at RT at several doses. STM images clearly demonstrated that the oxidation process was initiated at the termination side of the ribbons and was then propagating along the [-110] direction (Fig. 26). The formation of a SiO_2/Si interface with sub-oxides localized at the oxidation front was further confirmed by the de-convolution of the Si2p core-level [22]. The $I(V)$ spectra measured by STS on the oxidized Si NRs evidenced a small gap of 0.35 eV, revealing a semi-conducting behavior of this very thin (one layer) silicon oxide [22].

3.3. Silicene on Ag(111)

On the Ag(111) face, the deposition of one monolayer of silicon on the substrate held at a temperature of 250 °C was shown to produce a highly ordered honeycomb structure interpreted as a sheet of silicene epitaxied on silver [24]. This new structure of silicon grown on Ag surface is characterized by a $(2\sqrt{3}\times 2\sqrt{3})R30^\circ$ LEED pattern, indicating a long range order of the epitaxy. The atomic resolved STM images revealed the honeycomb structure formed by two silicon sublattices occupying positions at different heights, with a height difference of 0.02 nm (Fig. 27). A Si–Si nearest-neighbor distance of 0.19 ± 0.1 nm was derived from the analysis of the STM images, which is about 17% shorter than silicon bulk nearest neighbor value (0.235 nm).

4. Theoretical investigations of silicene

4.1. Tight-binding (TB) studies of silicene

To date, it appears that there are only two publications, which studied the silicene problem using an empirical TB theory [15,76]. The TB theory has been extremely useful and successful in the study of the electronic properties of graphene and of carbon nanotubes. As there are thousands of papers for the latter system we will cite only a few pioneering papers. An excellent review of the theory on carbon nanotubes can be found in the book by Saito and Dresselhaus [77]. In this section, we will start by presenting the basic elements of the TB theory, followed by a brief survey of applications to silicon-based systems. We will then summarize some of the key results for graphene and carbon nanotubes that have been obtained using this theory. Finally, we will review what has been obtained for silicene.

4.1.1. Tight-binding theory

The elements of the empirical TB theory were put forward by Slater and Koster [78]. In this formalism, the wave function is expanded as a Bloch sum of atomic-like orbitals:

$$|\Psi\rangle = \sum_{\alpha,A} C_{\alpha,A}|A,\alpha,k\rangle,$$

and

$$|A,\alpha,k\rangle = \frac{1}{\sqrt{N}}\sum_{i=1}^{N} e^{ik\cdot(R_i+\tau_A)}|R_i,A,\alpha\rangle,$$

where A represents inequivalent atoms in a unit cell, α labels the atomic-like basis, k is the wave vector, N is the number of unit cells, R_i labels the location of unit cells, and τ_A labels the atomic positions within a unit cell. Representation of the Hamiltonian in terms of Bloch sums of the atomic orbitals then leads to a matrix formulation with elements, $H^{AB}_{\alpha\beta}(k)$, which are functions of the wave vector of the periodic structure and of energy integrals:

$$\sum_{\beta,B} H^{AB}_{\alpha\beta}(k)\, C_{\beta,B} = E_n(k) C_{\alpha,A}.$$

In the empirical formulation, the energy integrals (so-called TB parameters) are not computed as in an *ab initio* theory, rather they are fitted to experimental data or other theories. The size of the matrix is given by the product of the number of inequivalent atoms, and the number of atomic orbitals used in the model. Diagonalization gives the electron energies, $E_n(k)$, or band structure, and the so-called TB envelope functions, $C_{\alpha,A}$. Note that the latter are not full wave functions; indeed, the full wave function is not explicitly obtained in the empirical TB method since the atomic orbitals, $|R_i,A,\alpha\rangle$, are not specified explicitly.

4.1.2. Bulk and nanostructured silicon

Much work has been carried out using the TB model for the tetrahedral semiconductors. We will here exclusively refer to some key work regarding silicon. Probably the first realistic description of the band structure of bulk silicon was due to Vogl et al. [79] whereby they were able to reproduce the indirect gap (about 1.1 eV along X direction in the first Brillouin zone) using a nearest-neighbor sp^3s^* model. Currently, one of the most sophisticated models is the nearest-neighbor $sp^3s^*d^5$ model due to Jancu et al. [80].

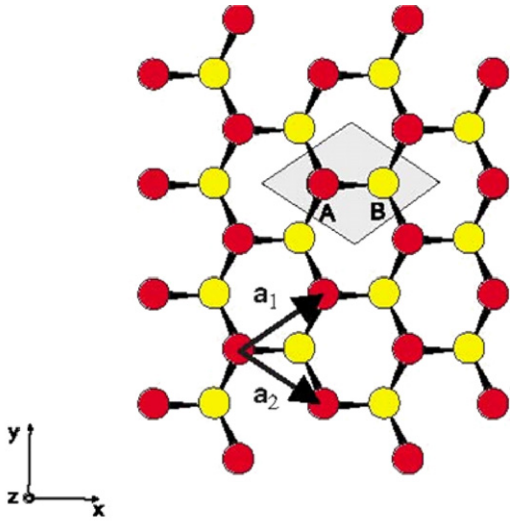

Fig. 28. Structure of graphene lattice [115].

Surfaces of silicon have also been studied, starting from unreconstructed but relaxed Si (111) surfaces [81] to total-energy calculations of surface structures [82]; for example, the 2 × 1 reconstruction of the Si (111) surface was verified. There is also a fair amount of literature on the study of the band structure of silicon superlattices [83], quantum dots [84], and nanowires [85].

4.1.3. Tight-binding results for graphene and carbon nanotubes

The TB model is developed as follows for graphene and carbon nanotubes. It is typical to separate the Hamiltonian for the π (p_z) electrons from that for the σ (sp^2) electrons. This is strictly valid only for a flat graphene sheet. Since the Dirac cones are only present in the π bands, it is now conventional to just consider the latter. There are two atoms in a unit cell (Fig. 28) and the Hamiltonian is then of size 2 × 2 in the absence of spin. The wave vector is two-dimensional for a single sheet. Note that there is no need to impose a super periodicity in the perpendicular direction (as is done with *ab initio* methods). It can be seen that the Hamiltonian is of very small size; indeed, it can be diagonalized exactly. The band structure of a nanotube can then be obtained from that of graphene by imposing an additional cyclic boundary condition in the direction of the chiral vector, which leads to an additional quantization. Thus, the wave vector is now becoming one-dimensional. The computational needs for computing the band structures of graphene and carbon nanotubes are negligible once the TB parameters are provided.

The analytical results provide some dramatic insight. Thus, the zero gap and a linear dispersion are both readily obtained, and clearly seen to be due to the similarity of the two inequivalent atoms, and to the symmetry of the 2D hexagonal lattice. Indeed, the above TB model leads to the following band structure for the π electrons:

$$E(k) = \pm\gamma\sqrt{1 + 4\cos\frac{\sqrt{3}k_x a}{2}\cos\frac{k_y a}{2} + 4\left(\cos\frac{k_y a}{2}\right)^2},$$

where a is the in-plane lattice constant, and γ is a transfer energy integral (−3.03 eV for graphene). The corresponding bands for both the π electrons and σ electrons are shown in Fig. 29.

For carbon nanotubes, the TB model leads immediately to the Hamada rule that describes the band gap variations with chirality [86]. Note that curvature effects are usually neglected in this model. The TB model has also been applied to graphene NRs and, although the initial models were incorrect, subsequent investigations have led to agreement with *ab initio* results by changing the edge TB parameters [87].

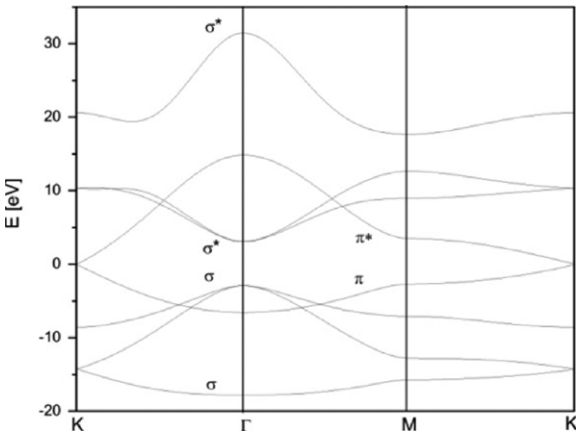

Fig. 29. Band structure of graphene [115].

Table 1
Fermi velocities of Dirac electrons.

Structure	v_F (m/s)
Graphene	$\sim 10^6$
α-silicene	$\sim 10^5$
β-silicene	$\sim 10^4$

4.1.4. Tight-binding results for silicene and silicon nanotubes

We finally discuss work related to the silicon nanostructures. We first note that, if the silicene sheet is flat (so-called α silicene), all of the theories and results discussed for graphene carry over. One simply replaces the graphene TB parameters by the silicon ones. However, it is known from *ab initio* calculations [88] that the most stable form of a 2D silicon sheet is buckled (β silicene). In this case, a different TB model needs to be derived. In Ref. [15], it was realized that β silicene is closely related to the structure of a monoatomic sheet of (111) silicon. This allowed them to derive a TB Hamiltonian closely related to the bulk Si Hamiltonian that reduces to the α silicene Hamiltonian when all the atoms are in the same plane. One consequence is the automatic coupling of the π and σ electrons leading to an 8 × 8 Hamiltonian [15]. The first important result is that the Dirac point is preserved even for β silicene [15]. This can be explained by the fact that the in-plane symmetry is unchanged. This is confirmed by the computed band structures (Fig. 30).

The TB results are semi-quantitatively similar to the *ab initio* ones of Yang and Ni [7]. Another result obtained by Guzmán-Verri and Lew Yan Voon is the Fermi velocity (Table 1).

4.1.5. Tight-binding results for silicane and hydrogenated silicon nanotubes

The band structure of fully hydrogenated silicene and silicon nanotubes has also been studied using the TB theory [76]. The TB parameters used are given in Table 2.

The band structure of silicane is shown in Fig. 31. The first result is that hydrogenation does not destroy the presence of Dirac points (at K), which has already been proven in an earlier paper by the same group [89]. Nevertheless, because of a band-filling effect, silicane has an indirect band gap (at M) which has been calculated to be around 2.2 eV using the TB model. It was also found that the near-gap states have a non-negligible amount of hydrogen s orbital but the Dirac points at K remain hydrogen free. For the silicon nanotubes, a new type of semiconductor has been proposed, one which presents equal and co-existing direct and indirect band gaps.

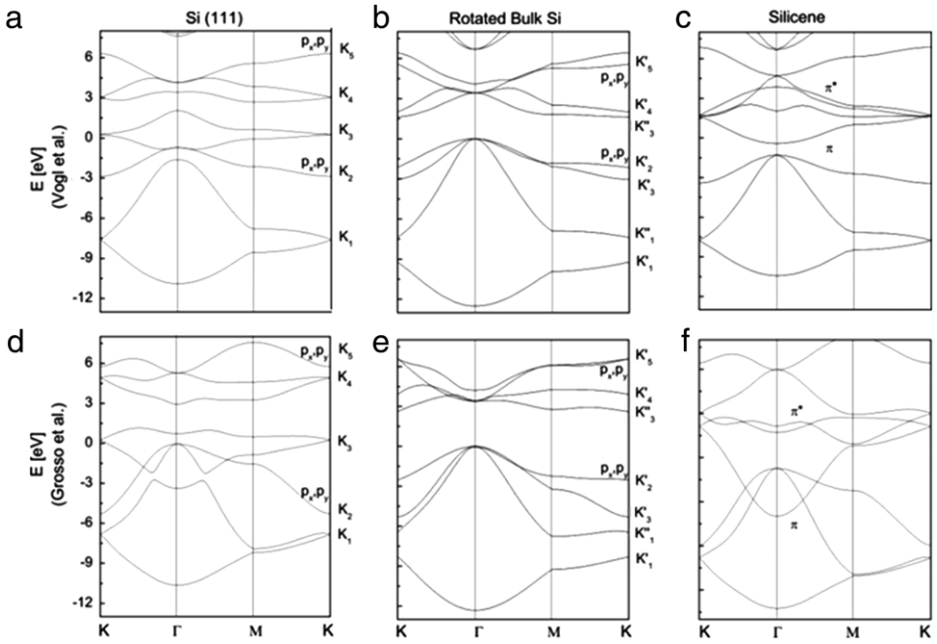

Fig. 30. Band structures of α-silicene (silicene) and β-silicene (Si(111)) using TB models, compared to rotated bulk Si band structures.

Table 2
Tight-binding parameters for hydrogenated silicene sheet.

Si–Si	in eV
E_s	−4.0497
E_p	1.0297
$(ss\sigma)_1^{AB}$	−2.0662
$(sp\sigma)_1^{AB}$	2.1184
$(pp\sigma)_1^{AB}$	3.1866
$(pp\pi)_1^{AB}$	−0.8867
$(ss\sigma)_2^{AA}$	0.0
$(sp\sigma)_2^{AA}$	0.0
$(pp\sigma)_2^{AA}$	0.8900
$(pp\pi)_2^{AA}$	−0.3612
Si–H	in eV
E_s (H)	13.6
$(sp\sigma)_1^{AC}$	6.2182

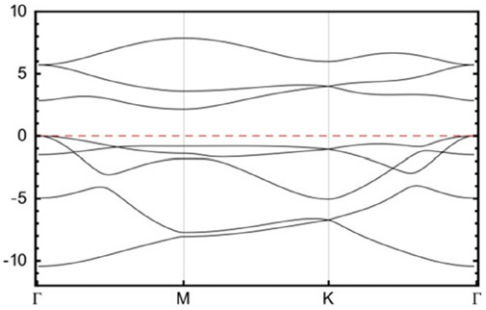

Fig. 31. Band structure of silicane using tight-binding.

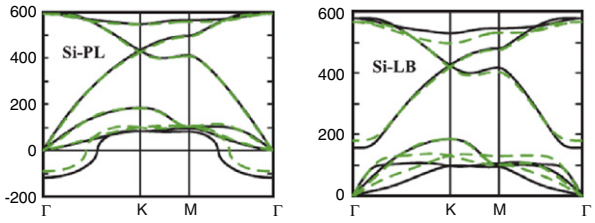

Fig. 32. The calculated phonon dispersions in planar (left) and LB structures (right) obtained by Cahangirov et al. [17] (courtesy of Cahangirov).

4.2. Density functional theory studies of silicene

4.2.1. "Bulk" silicene

The sp^2 hybridization in silicon has long been expected to be clearly unfavorable relative to the sp^3 forms, unlike in carbon where the two kinds of hybridizations, along with the sp^1, are closer in energy. A total-energy method, such as the density functional theory, is needed to discuss the relative stability of the different hybridizations.

Already in 1994 Takeda and Shiraishi studied the crystalline structure of silicene and germacene [88]. They confirmed graphene to be stable in the planar layer, but silicene and germacene to buckle. Their calculated band structure of silicene showed the Dirac cone at the Fermi energy at the k-point K, with a linear dispersion around it, like in graphene despite the lower symmetry of D_{3h} instead of D_{6h} in graphene.

The total energy calculations by Cahangirov et al. [17] and Ding and Ni [90] provided insight into the geometric and electronic structure of the silicene and germacene layers. The two groups also showed that the planar honeycomb lattice, the ground state of graphene, of Si or Ge is unstable toward a distortion of the layer due to an imaginary phonon mode, shown in Fig. 32 from the work by Cahangirov et al. [17].

Further, the same authors found two different minima in the total energy versus the lattice constant, as seen in Fig. 33a [91]. The two structures are characterized by a low-buckling (LB) structure with a lattice constant of ca. 0.39 nm and the high-buckling (HB) of ca. 0.27 nm, as shown in Fig. 33b.

Our own calculations using the generalized gradient approximation (GGA) functional show very similar shapes of the minima around the LB and HB structures compared to local density approximation (LDA), but the LB minimum is slightly preferred. The buckling, or the height difference between the two atoms in the unit cell, displays a monotonous increase when the lattice constant is

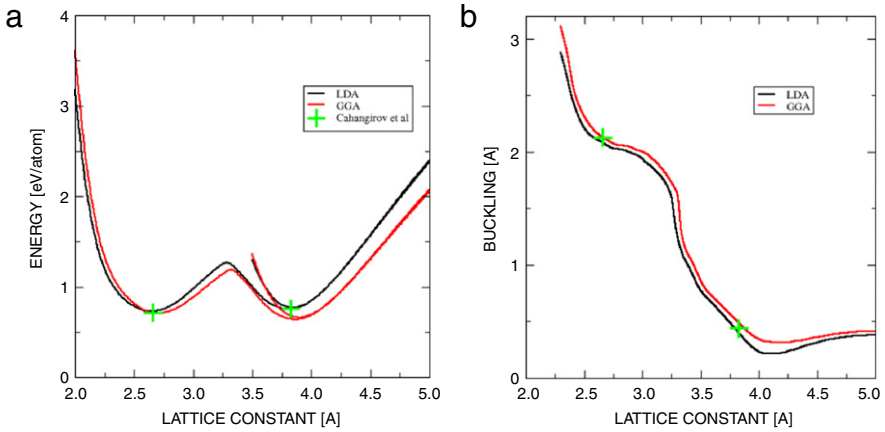

Fig. 33. (a) The energy per atom relative to the diamond structure as a function of the lattice constant; (b) the buckling of the two atoms in the honeycomb structure obtained by geometry optimization. The crosses mark the results of Cahangirov et al. [17] using LDA.

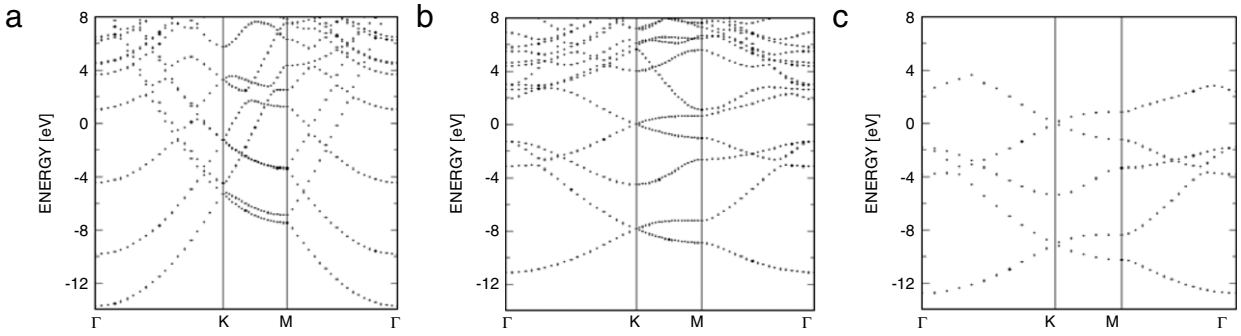

Fig. 34. The electronic band structure calculated using GGA–PBE in the (a) HB, (b) LB structures, and (c) HSE06 hybrid functional in the LB structure (the geometry is taken from the GGA–PBE calculation).

decreased below 0.40 nm. Both LDA and GGA yield very similar buckling; at the GGA level the buckling is 0.215 and 0.045 nm in the HB and LB structures, respectively. Even at extended lattice constants we do not find that the buckling would vanish, demonstrating a clear preference of the sp^3 over sp^2 hybridization.

The band structure in the LB and HB structures is displayed in Fig. 34. For the band structure of the HB geometry (Fig. 34a), the Fermi energy is crossed by several bands, and there is no signature of a Dirac cone. On the contrary the LB (Fig. 34b) presents a Dirac cone and resembles that of graphene. The σ bands closest to the Fermi energy are at -1.3 and $+1$ eV. Considering the typical contraction (reduction) of the Kohn–Sham eigenvalues by 50%, we expect the real σ–σ band gap to be about 4 eV; indeed, the HSE hybrid-exchange–correlation functional that is in general more accurate for the band structures yields a value of 4.25 eV, and the width, or the distance from the bottom of the valence band to the Fermi energy of 12.76 eV (Fig. 34c).

The buckling of the germacene layer was also found by Takeda and Shiraishi [88]. Lebègue and Eriksson [16] and Houssa et al. [92] found the band structure to be similar to the case of graphene and silicene, but the Fermi surface is cut by another band at the Γ point; they did not include the corrugation of the germacene layer though. Later Cahangirov et al. [17] and Lew Yan Voon et al. [89] recalculated the band structure with corrugation and found no extra states crossing the Fermi energy. The Fermi velocity calculated by Lew Yan Voon et al. [89] in graphene, silicene and germacene, 6.3×10^5, 5.1×10^5 and 3.8×10^5 m/s, respectively, are relatively similar in magnitude. The elastic constants of silicene, germacene and other two-dimensional crystals were calculated first by Wang [74], and very recently Cheng, Zhu and Schwingenschlögl [93] calculated the effects of charge carrier doping on the properties of silicene.

4.2.2. Adsorption of hydrogen on silicene

The experiments on the supported silicene layers have demonstrated that the silicon atoms are not reactive toward molecular oxygen. A similar test on reactivity can be performed for adsorption of hydrogen in the electronic-structure calculations. We studied therefore the binding energy of single hydrogen atoms on silicene with DFT–GGA, and found a binding energy of 3 meV and -2.40 eV on the high- and low-buckled layer, respectively. The latter value indicates that the adsorption of a single hydrogen atom on the silicene surface is not thermodynamically stable, if compared to the energy in gaseous hydrogen. Thus the silicene surface is not reactive toward dissociation of hydrogen, indicating a passive surface.

The hydrogenated surface of silicene, "silicane" in analogy with graphane, was investigated by Takeda and Shiraishi [94] using DFT–LDA methodology. Lew Yan Voon et al. [89] performed DFT–LDA calculations on the hydrogenated graphene, silicene and germacene. The results are collected into Table 3. It is interesting that the lateral lattice constant a of silicene does not change upon the hydrogenation, and also the Si–Si distance increases only little. The Si–H binding energy is, however, similar to the silicane and thus is relatively strong resulting in a reactive silicene layer is reactive toward adsorption of atomic hydrogen. The band structure of silicane, shown in Fig. 35, reveals an indirect band gap of about 2 eV in the LDA calculations. Therefore in reality the gap would be about 3–4 eV. Overall the band structure resembles the one of graphane.

We note that Lew Yan Voon et al. used the local density approximation to calculate the binding energies shown in Table 3. In our new calculations employing the GGA-PBE the hydrogen was bound much less in the low-buckled silicane structure, 2.08 eV relative to hydrogen atom (unbound by 0.2 eV relative

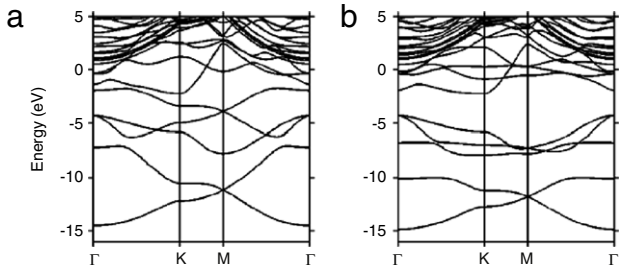

Fig. 35. The band structure of (a) silicene and (b) silicane using DFT-LDA method. From Ref. [89].

Table 3
The hexagonal lattice constant a, distance between the host atoms d_{IV-IV}, vertical buckling Δz and host-hydrogen distance d_{IV-H} in graphene, graphane, silicene, silicane, germacene and germacane. Values from Ref. [89] in Å for lengths and eV for energies.

	a	d_{IV-IV}	Δz	d_{IV-H}	E_{-b}
Graphene	2.45	1.41	0		
Graphane	2.51	1.52	0.45	1.08	3.68
Silicene (LB)	3.82	2.25	0.44		
Silicane (LB)	3.82	2.32	0.72	1.50	3.16
Germacene (LB)	4.0	2.38	0.71		
Germacane (LB)		2.34	0.69	1.53	2.8

to a hydrogen atom in hydrogen dimer) compared to 3.16 eV by Lew Yan Voon et al. In their new article, Osborn et al. [95] also used the DFT–GGA approach and obtained values similar to ours at the low hydrogen coverage. The values show that the silicane structure could be prepared by using atomic hydrogen, but it would be thermodynamically unstable against desorption of hydrogen, again demonstrating low reactivity toward common gases. Recently Garcia et al. [96] have further studied the fluorinated silicene.

4.2.3. Silicene nanoribbons

The electronic components built from silicene would require a band gap to function. Since bulk silicene is a semi-metal, with the Dirac cone at the Fermi energy, one way to achieve the opening of the gap is to restrict the geometry into one dimension: this can be manufactured by constructing nanoribbons, i.e. cutting the two-dimensional plane into stripes with a finite width. Cahangirov et al. [17] performed total energy calculations for the armchair- and zigzag-oriented nanoribbons without adatoms. They found a reconstruction in both types of the cuts when two unit cells along the ribbon were allowed to relax without a symmetry constraint. Ding and Ni [90] investigated hydrogen terminated armchair- and zigzag-oriented nanoribbons. The results from their study are shown in Fig. 36. Like in the graphene nanoribbons, the narrow ribbons exhibit a band gap that varies with the width of the ribbons in an oscillatory manner. The zigzag ribbon shows also ferromagnetism along the edge (opposing spins at the opposite edges of the NR) that opens a small gap around the Fermi energy.

4.2.4. Further studies on bulk silicene

Further calculations on bulk silicene and germacene have been published in [97–102], and on silicene and germacene nanoribbons [103–108]. Other calculations of the structure of single (SL) and double layers (DL) of silicon were carried out by Morishita et al. [109–111]. In the first paper, they performed molecular dynamics (MD) simulations of silicon atoms confined between parallel planes. The interaction between the silicon atoms was described by the Tersoff potential and the atoms interacted with the walls via a Lennard-Jones potential. They obtained a hexagonal structure for both the single and double layers. In particular, they found the single layer to be flat with a bond length of 2.31 Å. The bond length is larger than for other studies, and the fact that they found the structure to be flat is likely a consequence of the confinement imposed. In [110], they used DFT–GGA to further study the properties of DL–Si under hydrogenation. They found the bond length to increase, as was also found by Lew Yan Voon et al. [89] for silicane. They also obtained a band gap of 1.2 eV for DL–Si:H, compared to the 2.0 eV band gap for SL–Si:H (silicane) [89]. Finally, in [111], the authors reported a surface reconstruction for SL–Si, a Si(111)-2×2 structure, using MD calculations.

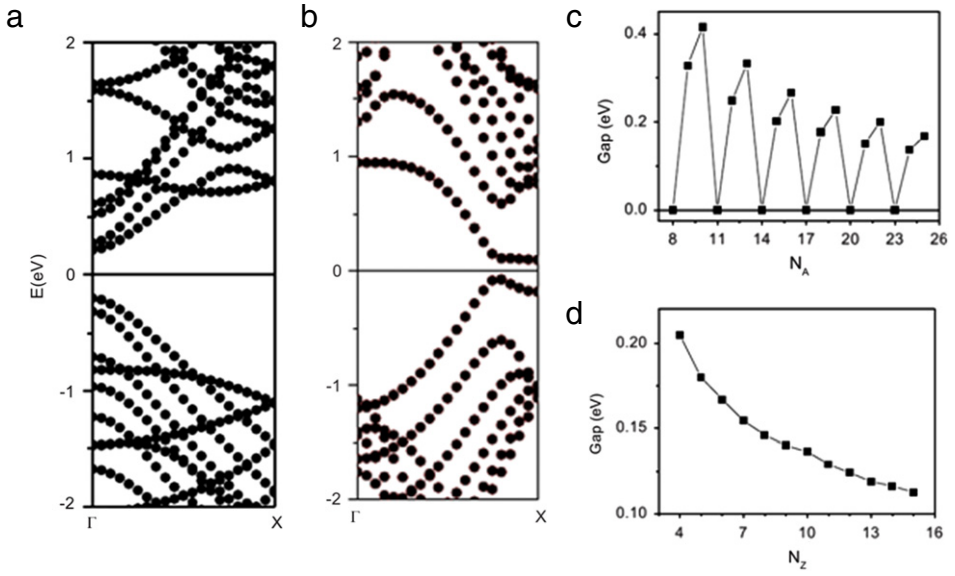

Fig. 36. The band structure of a singly hydrogen-terminated silicene nanoribbon with: (a) armchair edge of width 10 (10 different C–C bonds along the ribbon); (b) zigzag edge of width 6 (6 zigzag chains along the ribbon) in the anti-ferromagnetic spin coupling. The band gap of silicene nanoribbons with (c) armchair and (d) zigzag edge as a function of the width of the nanoribbons (courtesy of Ni).
Source: From Ref. [90].

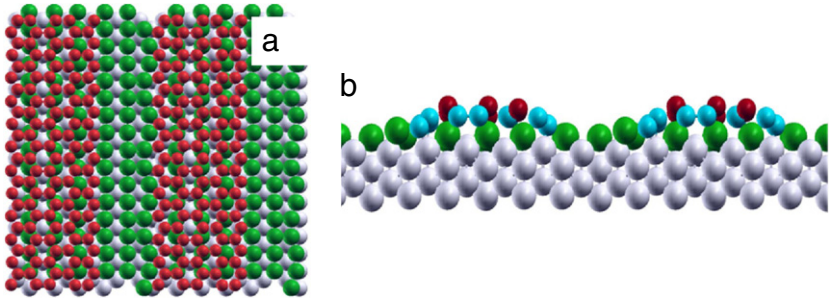

Fig. 37. (a) Top view of Si nano-ribbons on Ag(110): (a) silicon atoms (red) forming hexagons along the channels on top of the surface Ag atoms (green); (b) side view of Si (red and blue) nano-ribbons on Ag(110) showing the arched structure of the ribbons. (For interpretation of the references to colour in this figure legend, the reader is referred to the web version of this article.)

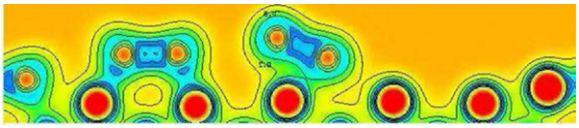

Fig. 38. Calculated charge density in cross section for the silicon nano-ribbons shown in Fig. 37. (For interpretation of the references to colour in this figure legend, the reader is referred to the web version of this article.)

4.2.5. DFT investigations of adsorbed silicene on silver surfaces

There are only two groups who studied the adsorption of silicene on silver surfaces using density functional theory, namely Kara et al. who investigated silicene NRs and sheets on Ag(110) [23,26] and Ag(111) [112], and He who investigated the cases of Si/Ag(110) [113] and Si/Ag(100) [114]. The first study of Si/Ag(110) was done by He [113] who has calculated several adsorption geometries for Si coverage up to 2 monolayers. He found that silicon is stable as a superstructure on Ag(110). However, the one monolayer Si structure this used by He did not show agreement with the experimental data. In his model, He used silicon atoms in a rectangular arrangement instead of the observed hexagonal one; as a consequence, this arrangement presents a mirror symmetry that is in contradiction with the observed symmetry breaking in the [00-1] direction which is clearly observed experimentally by our STM measurements, as clearly shown in Fig. 19.

Kara and his collaborators have performed more in depth investigation of Si NRs on Ag(110) [23,26]. In their simulations, they considered several structures where silicon atoms where always arranged in a honeycomb structure. The number of atoms per unit cell varied between 28 and 36 silicon atoms. Using the signatures present in the STM figures shown in Figs. 19 and 20, namely an asymmetry of the ribbon profile and the presence of bright spots representing a rectangle and a diamond, Kara et al. [26] proceeded by elimination and found that only the configuration with 30 silicon atoms shows an excellent agreement with the experimental observation. The Si30 configuration is shown in Fig. 37a.

Note that the silicon atoms do not sit at the same height but rather forming an arched structure as shown in Fig. 37b. This non-equivalency in the position of the silicon atoms is responsible for the appearance of the rectangle and diamond shapes in the STM images, as depicted in Fig. 22. The asymmetry shown in Fig. 19 is also reproduced by the work of Kara et al. [23] in terms of an asymmetry in the charge density in a plane perpendicular to the direction of the ribbons (Fig. 38).

It is this geometrical asymmetry in the NRs that is responsible for the dip in the electronic density profile shown in Fig. 19. Kara et al. argued that it is this dip that is responsible for the rapid growth of the NRs. Indeed, the dip in the density is also a dip in the energy landscape that a diffusing silicon atom would encounter. Once a Si atom is attached to the side of a NR, since it will be in a deep well, it will rapidly diffuse along the side of the ribbon and attach to the extremity, contributing to the anisotropic growth of the ribbon. This was labeled by the authors as the "gutters effect" and may be applied to the growth of other one dimensional systems.

5. Conclusion

Though the number of independent experimental investigations on silicene is limited, there is a clear indication that silicon may form a "quasi-2D" structure resembling that of graphene. The main experimental evidence relies on detailed, high resolution STM images of epitaxial growth of silicon on silver surfaces. On Ag(110), silicene grows as nanoribbons of a single width, which is 4 times the lattice constant of silver. These NRs extend hundreds of nanometers in length and appear to have their edges resistant to oxygen. A preliminary photo-emission investigation of the electronic structure of silicene NRs, as adsorbed on Ag(110) revealed a linear behavior in the band structure along the ribbon, indicating a possibility that the electronic properties of these NRs may resemble those of graphene. On Ag(111), STM images show silicene sheets grown over very large surface areas. More detailed experimental investigations of the atomic and the electronic structures of silicene, as grown on silver surfaces, are much needed. Theoretical investigations of bulk silicene (standalone) showed that unlike graphene, silicene has a slight buckling of about 0.4 Å. These studies also predict a substantial reduction of the nearest-neighbor distance, which was predicted to be 2.2 Å. The calculated electronic, magnetic and chemical properties of silicene were found to follow the same trends as graphene, which make silicene a viable candidate for electronic devices.

Finally, contrary to graphene that can be formed as standalone sheets and ribbons, silicene has only been grown on metal surfaces (on silver so far). In addition, given the tendency of silicon to form an sp^3 bond, silicene will always need a substrate for epitaxial growth. Hence, to push silicene to the next step as a new candidate for electronics, it is necessary to grow silicene sheets and NRs on insulators or metal surfaces covered with insulator thin films. Silicon in the form of silicene may form a fairly new avenue for an old player in the electronic industry, which will hopefully extend the lifetime of Moore's law.

Acknowledgments

AK thanks the University of Central Florida for partial support through an Inhouse grant, the University of Cergy Pontoise for hospitality, and Dr. Handan Yildirim for fruitful discussions and a critical reading of the manuscript. We are indebted to Professor Thomas Greber for his continuous support on this subject. We would like also to acknowledge constructive discussions with Gerald Dujardin, Hung Diep, Guy Treglia, Guy Lelay and Benedicte Ealet.

References

[1] K.S. Novoselov, A.K. Geim, S.V. Morozov, D. Jiang, Y. Zhang, S.V. Dubonos, I.V. Grigorieva, A.A. Firsov, Science 306 (2004) 666.
[2] K.S. Novoselov, D. Jiang, F. Schedin, T.J. Booth, V.V. Khotkevich, S.V. Morozov, A.K. Geim, Proc. Natl. Acad. Sci. USA 102 (2005) 10451.
[3] K.S. Novoselov, A.K. Geim, S.V. Morozov, D. Jiang, M.I. Katsnelson, I.V. Grigorieva, S.V. Dubonos, A.A. Firsov, Nature 438 (2005) 197.
[4] A.K. Geim, K.S. Novoselov, Nature Mater. 6 (2007) 183.
[5] U. Röthlisberger, W. Andreoni, M. Parrinello, Phys. Rev. Lett. 72 (1994) 665.
[6] S.B. Fagan, R.J. Baierle, R. Mota, Z.J.R. da Silva, A. Fazzio, Phys. Rev. B 61 (2000) 9994.
[7] Xiabao Yang, Jun Ni, Phys. Rev. B 72 (2005) 195426.
[8] Y.H. Tang, L.Z. Pei, Y.W. Chen, C. Guo, Phys. Rev. Lett. 95 (2005) 116102.
[9] M.D. Crescenzi, P. Castrucci, M. Scarselli, M. Diociaiuti, P.S. Chaudhari, C. Balasubramanian, T.M. Bhave, S.V. Bhoraskar, Appl. Phys. Lett. 86 (2005) 231901.
[10] S. Yamada, H. Fujiki, Jap. J. Appl. Phys. 45 (2006) L837.
[11] H. Nakano, T. Mitsuoka, M. Harada, K. Horibuchi, H. Nozaki, N. Takahashi, T. Nonaka, Y. Seno, H. Nakamura, Angew. Chem. 45 (2006) 6303.
[12] H. Okamoto, Y. Kumai, Y. Sugiyama, T. Mitsuoka, K. Nakanishi, T. Ohta, H. Nozaki, S. Yamaguchi, S. Shirai, H. Nakano, J. Am. Chem. Soc. 132 (2010) 2710.
[13] Y. Sugiyama, H. Okamoto, T. Mitsuoka, T. Morikawa, K. Nakanishi, T. Ohta, H. Nakano, J. Am. Chem. Soc. 132 (2010) 5946.
[14] J. Kim, Y.H. Kim, S.-H. Choi, W. Lee, ACS Nano 5 (2011) 5242.
[15] G.G. Guzmán-Verri, L.C. Lew Yan Voon, Phys. Rev. B 76 (2007) 075131.
[16] S. Lebègue, O. Eriksson, Phys. Rev. B 79 (2009) 115409.
[17] S. Cahangirov, M. Topsakal, E. Aktürk, H. Sahin, S. Ciraci, Phys. Rev. Lett. 102 (2009) 236804.
[18] C. Léandri, H. Oughaddou, B. Aufray, J.M. Gay, G. Le Lay, A. Ranguis, Y. Garreau, Surf. Sci. 601 (2007) 262.
[19] C. Léandri, G. Le Lay, B. Aufray, C. Girardeaux, J. Avila, M.E. Davila, M.C. Asensio, C. Ottaviani, A. Cricenti, Surf. Sci. 574 (2005) L9.
[20] G. Le Lay, B. Aufray, C. Léandri, H. Oughaddou, J.-P. Bibérian, P. De Padova, M.E. Dávila, B. Ealet, A. Kara, Appl. Surf. Sci. 256 (2009) 524.
[21] A. Kara, C. Léandri, M.E. Dávila, P. De Padova, B. Ealet, H. Oughaddou, B. Aufray, G. Le Lay, J. Supercond. Novel Magn. 22 (2009) 259.
[22] P. De Padova, C. Léandri, S. Vizzini, C. Quaresima, P. Perfetti, B. Olivieri, H. Oughaddou, B. Aufray, G. Le Lay, Nano Lett. 8 (2008) 2299.
[23] B. Aufray, A. Kara, S. Vizzini, H. Oughaddou, C. Léandri, B. Ealet, G. Le Lay, Appl. Phys. Lett. 96 (2010) 183102.
[24] B. Lalmi, H. Oughaddou, H. Enriquez, A. Kara, S. Vizzini, B. Ealet, B. Aufray, Appl. Phys. Lett. 97 (2010) 22310.
[25] P. De Padova, C. Quaresima, C. Ottaviani, P.M. Sheverdyaeva, P. Moras, C. Carbone, D. Topwal, B. Olivieri, A. Kara, H. Oughaddou, B. Aufray, G. Le Lay, Appl. Phys. Lett. 96 (2010) 261905.
[26] A. Kara, S. Vizzini, C. Léandri, B. Ealet, H. Oughaddou, B. Aufray, G. Le Lay, J. Phys.: Condens. Matter 22 (2010) 045004.
[27] U. Bardi, Rep. Progr. Phys. 57 (1994) 939.
[28] F. Ducastelle, B. Legrand, G. Tréglia, Progr. Theor. Phys. 101 (Suppl.) (1990) 159.
[29] J. du Plessis, Solid State Phenom. 11 (1990) 1.
[30] P. Wynblatt Ed. (Ed.), Modeling of Segregation Phenomena at Alloy Surface Computational Materials Science, 1999.
[31] P. Wynblatt, R.C. Ku, Surf. Sci. 65 (1977) 511.
[32] G. Tréglia, B. Legrand, F. Ducastelle, Europhys. Lett. 7 (1988) 575.
[33] J. Eugène, B. Aufray, F. Cabané, Surf. Sci. 241 (1991) 1.
[34] Y. Liu, P. Wynblatt, Surf. Sci. 240 (1990) 245.
[35] H. Giordano, O. Alem, B. Aufray, Scr. Metall. 28 (1993) 257.
[36] I. Meunier, J.M. Gay, L. Lapena, B. Aufray, H. Oughaddou, E. Landemark, G. Falkenberg, L. Lottermoser, R.L. Johnson, Surf. Sci. 422 (1999) 42.
[37] H. Giordano, B. Aufray, Surf. Sci. 816 (1994) 307–309.
[38] G. Tréglia, B. Legrand, J. Eugène, B. Aufray, F. Cabané, Phys. Rev. B 44 (1991) 5842.
[39] H. Giordano, B. Aufray, Surf. Sci. 280 (1996) 352–354.
[40] A. Saùl, B. Legrand, G. Treglia, Phys. Rev. B 50 (1994) 1912.
[41] R. Dudde, H. Bernhoff, B. Reihl, Phys. Rev. B 41 (1990) 12029.
[42] M. Göthelid, M. Hammar, M. Björkqvist, U.O. Karlson, S.A. Flodström, C. Wigren, G. Lelay, Phys. Rev. B 50 (1994) 4470.
[43] M. Hammar, M. Göthelid, U.O. Karlson, S.A. Flodström, Phys. Rev. B 47 (1993) 15669.
[44] D. Dornish, W. Moritz, H. Schulz, R. Feidenhans'l, M. Nielsen, F. Grey, R.L. Johnson, G. Lelay, Surf. Sci. 274 (1992) 215–221.
[45] G. Lelay, R.L. Johnson, R. Seemann, F. Grey, R. Feidenhans'l, M. Nielsen, Surf. Sci. 287 (1993) 539–544.
[46] J. Nogami, A.A. Baski, C.F. Quate, Phys. Rev. Lett. 65 (1990) 1611.
[47] Y. Chang, Y. Hwu, J. Hansen, F. Zanini, G. Margaritondo, Phys. Rev. Lett. 63 (1989) 1845.
[48] D.W. Niles, N. Tache, D.G. Kilday, M.K. Kelly, G. Margaritondo, Phys. Rev. B 34 (1986) 967.
[49] M.W. Ruckman, J.J. Joyce, F. Boschereni, J.H. Weaver, Phys. Rev. B 34 (1986) 5118.
[50] J.A. Martín-Gago, R. Fasel, J. Hayoz, R.G. Agostino, D. Naumovi, P. Aebi, L. Schlapbach, Phys. Rev. B 55 (1997) 12896;
C. Polop, C. Rojas, J.A. Martín-Gago, R. Fasel, J. Hayoz, D. Naumovi, P. Aebi, Phys. Rev. B. 63 (2001) 115414.
[51] D.E. Bürgler, P. Hermann, S. Corbel, C.M. Schmidt, D.M. Schaller, P. Sautet, A. Baratoff, H-J Güntherodt, Phys. Rev. B 57 (1998) 10035.
[52] C. Polop, J.L. Sacedón, J.A. Martín-Gago, Surf. Sci. (1998) 245–248.
[53] C. Polop, C. Rojas, E. Roman, J.A. Martín-Gago, B. Brena, D. Cocco, G. Paolucci, Surf. Sci. 407 (1998) 268–274.
[54] J.A. Martín-Gago, C. Rojas, C. Polop, J.L. Sacedón, E. Romàn, Phys. Rev. B 59 (1999) 4.
[55] T.B. Massalski, Binary Alloy Phase Diagrams, 2nd ed., Materials Society, 1992.
[56] R.W. Olesinski, G.J. Abbaschian, Bull. Alloy Phase Diagr. 9 (1988) 59.
[57] H. Oughaddou, B Aufray, J.P. Bibérian, J.Y. Hoarau, Surf. Sci 429 (1999) 320.
[58] H. Oughaddou, J.M. Gay, B. Aufray, L. Lapena, G. Le Lay, O. Bunk, G. Falkenberg, J.H. Zeysing, R.L. Johnson, Phys. Rev. B 61 (2000) 5692.
[59] H. Oughaddou, B. Aufray, J.-P. Bibérian, B. Ealet, G. Le Lay, G. Tréglia, A. Kara, T.S. Rahman, Surf. Sci. 602 (2008) 506.
[60] C. Léandri, H. Oughaddou, J.M. Gay, B. Aufray, G. Le Lay, J.P Bibérian, A. Rangüis, O. Bunk, R.L. Johnson, Surf. Sci. L573 (2004) L369.
[61] H. Oughaddou, S. Sawaya, J. Goniakowski, B. Aufray, G. Tréglia, G. Le Lay, J.M. Gay, N. Barrett, C. Guillot, A. Mayne, G. Dujardin, Phys. Rev. B 62 (2000) 16653.
[62] H. Oughaddou, B. Aufray, J.M. Gay, Sur. Rev. Lett. 6 (1999) 929.
[63] H. Oughaddou, A. Mayne, B. Aufray, J.P. Bibérian, G. Le Lay, B. Ealet, G. Dujardin, A. Kara, J. Nanosci. and Nanotechn. 7 (2007) 3189.
[64] H. Oughaddou, C. Léandri, B. Aufray, G. Le Lay, Proceedings of Advanced Semiconductor Devices and Microsystems, 2004. ASDAM 2004. The Fifth International Conference on ASDAM'04, IEEE, ASDAM'04, ISBN: 0-7803-8335-7, 33-39, 2004.
[65] H. Oughaddou, B. Aufray, G. Le Lay, J.M. Gay, J. Zeysing, R.L. Johnson, Appl. Surf. Sci. 162 (2000) 74–77.
[66] J. Dalmas, H. Oughaddou, C. Léandri, J-M. Gay, G. Le lay, G. Tréglia, B. Aufray, O. Bunk, R.L. Johnson, Phys. Rev. B 72 (2005) 155424.
[67] J. Dalmas, H. Oughaddou, G. Le Lay, B. Aufray, G. Tréglia, C. Girardeaux, J. Bernardini, Jun Jujii, G. Panaccione, Surf. Sci. 600 (2006) 1227.
[68] J. Dalmas, H. Oughaddou, C. Léandri, J.M. Gay, G. Le lay, G. Tréglia, B. Aufray, O. Bunk, R.L. Johnson, J. Phys. Chem. Solids 67 (2006) 601.
[69] C. Leandri, H. Saifi, O. Guillermet, B. Aufray, App. Surf. Sci. 177 (2001) 303.
[70] H. Sahaf, L. Masson, C. Léandri, B. Aufray, G. Le Lay, F. Ronci, Appl. Phys. Lett. 90 (2007) 263110.
[71] P. De Padova, C. Quaresima, P. Perfetti, B. Olivieri, C. Leandri, B. Aufray, S. Vizzini, G. Le Lay, NanoLett. 8 (2008) 271.
[72] M.A. Valbuena, J. Avila, M.E. Davila, C. Léandri, B. Aufray, G. Le Lay, M.C. Asensio, Appl. Surf. Sci. 254 (2007) 50.
[73] E. Salomon, A. Kahn, Surf. Sci. 602 (2008) L79.
[74] Shaoqing Wang, J. Phys. Soc. Japan 79 (2010) 064602.
[75] P.R. Bandaru, P. Pichanusakorn, Semicond. Sci. Technol. 25 (2010) 024003.
[76] G.G. Guzmán-Verri, L.C. Lew Yan Voon, J. Phys. Cond. Matter 23 (2011) 145502.
[77] R. Saito, G. Dresselhaus, M.S. Dresselhaus, Physical Properties of Carbon Nanotubes, Imperial College Press, London, 1998.
[78] J.C. Slater, G. Koster, Phys. Rev. 94 (1954) 1498.
[79] P. Vogl, H.P. Hjalmarson, J.D. Dow, J. Phys. Chem. Sol. 44 (1983) 365.
[80] J.-M. Jancu, R. Scholz, F. Beltram, F. Bassani, Phys. Rev. B 57 (1998) 6493.
[81] K.C. Pandey, J.C. Phillips, Phys. Rev. Lett. 34 (1450) 1975.
[82] D.J. Chadi, Phys. Rev. Lett. 41 (1978) 1062.
[83] T.P. Pearsall, L. Colace, A. DiVergilio, W. Jager, D. Stenkamp, G. Theodorou, H. Presting, E. Kasper, K. Thonke, Phys. Rev. B 57 (1998) 9128.
[84] J. See, P. Dolfus, S. Galdin, Phys. Rev. B 66 (2002) 193307.
[85] A. Svizhenko, P.W. Leu, K. Cho, Phys. Rev. B 75 (2007) 125417.
[86] N. Hamada, S.I. Sawada, A. Oshiyama, Phys. Rev. Lett. 68 (1992) 1579.
[87] H. Zheng, Z.F. Wang, T. Luo, Q.W. Shi, J. Chen, Phys. Rev. B 75 (2007) 165414.
[88] K. Takeda, K. Shiraishi, Phys. Rev. B 50 (1994) 14916.
[89] L.C. Lew Yan Voon, E. Sandberg, R.S. Aga, A.A. Farajian, Appl. Phys. Lett. 97 (2010) 163114.
[90] Yi Ding, Jun Ni, Appl. Phys. Lett. 95 (2009) 083115.
[91] We performed DFT calculations using the Quantum ESPRESSO plane wave code [116]. Vanderbilt ultra-soft pseudo potentials were used to describe and action of the nuclei and core electrons on the valence electrons in the interatomic regions. The single-electron wave functions and electronic density were expanded in the plane wave basis set up to a 35 and 300 Ry, respectively. The atomic buckling was optimised until the forces on the nuclei were vanishingly small. A vacuum of at least 16 Å was used to separate the 2D layers. We employed LDA, GGA in the parametrisation PBE [117] and HSE06 range-separated hybrid exchange functionals [118].
[92] M. Houssa, G. Pourtois, V.V. Afanas'ev, A. Stesmans, Appl. Phys. Lett. 96 (2010) 082111.
[93] Y.C. Cheng, Z.Y. Zhu, U. Schwingenschlögl, EPL 95 (2011) 17005.
[94] K. Takeda, K. Shiraishi, Phys. Rev. B 39 (1989) 11028.
[95] T.H. Osborn, A.A. Farajian, O.V. Pupysheva, R.S. Aga, L.C. Lew Yan Voon, Chem. Phys. Lett. 511 (2011) 101–105.
[96] J.C. Garcia, D.B. de Lima, L.V.C. Assali, J.F. Justo, J. Phys. Chem. C. (in press).
[97] G. Seifert, Th. Köhler, H.M. Urbassek, E. Hernández, Th. Frauenheim, Phys. Rev. B 63 (2001) 193409.
[98] H. Sahin, S. Cahangirov, M. Topsakal, E. Bekaroglu, E. Aktürk, R.T. Senger, S. Ciraci, Phys. Rev. B 80 (2009) 155453.
[99] N.Y. Dzade, K.O. Obodo, S.K. Adjokatse, A.C. Ashu, E. Amankwah, C.D. Atiso, A.A. Bello, E. Igumbor, S.B. Nzabarinda, J.T. Obodo, A.O. Ogbuu, O.E. Femi, J.O. Udeigwe, U.V. Waghmare, J. Phys. Condens. Matter 22 (2010) 375502.

[100] M. Houssa, G. Pourtois, V.V. Afanas'ev, A. Stesmans, Appl. Phys. Lett. 97 (2010) 112106.
[101] M. Houssa, G. Pourtois, M.M. Heyns, V.V. Afanas'ev, A. Stesmans, J. Electrochem. Soc. 158 (2011) H107.
[102] H. Behera, G. Mukhopadhyay, in: D.K. Aswal, A.K. Debnath (Eds.), Proceedings of International Conference on Physics of Emerging Functional Materials PEFM-2010.
[103] Y.-L. Song, Y. Zhang, J.-M. Zhang, D.-B. Lu, Appl. Surf. Sci. 256 (2010) 6313.
[104] M. Miller, F.J. Owens, Chem. Phys. 381 (2011) 1.
[105] Y.-L. Song, Y. Zhang, J.-M. Zhang, D.-B. Lu, K.-W. Xu, Physica B 406 (2011) 69.
[106] Y.-L. Song, Y. Zhang, J.-M. Zhang, D.-B. Lu, K.-W. Xu, Europ. Phys. B 79 (2011) 197.
[107] S. Cahangirov, M. Topsakal, S. Ciraci, Phys. Rev. B. 81 (2010) 195120.
[108] Y.-L. Song, Y. Zhang, J.-M. Zhang, D.-B. Lu, K.-W. Xu, J. Mol. Struct. 75 (2011) 990.
[109] T. Morishita, K. Nishio, M. Mikami, Phys. Rev. B 77 (2008) 081401.
[110] T. Morishita, S.P. Russo, I.K. Snook, M.J.S. Spencer, K. Nishio, M. Mikami, Phys. Rev. B 82 (2010) 045419.
[111] T. Morishita, M.J.S. Spencer, S.P. Russo, I.K. Snook, M. Mikami, Chem. Phys. Lett. 506 (2011) 221.
[112] A. Kara, H.B. Enriquez, S. Vizzini, B. Ealet, B. Aufray, H. Oughaddou, Global J. Phys. Chem. 2 (2011) 145.
[113] G.M. He, Phys. Rev. B 73 (2006) 035311.
[114] G.M. He, Surf. Sci. 603 (2009) 2021.
[115] G.G. Guzmán-Verri, Electronic Properties of Silicon-Based Nanostructures MS thesis, Wright State University, Dayton, 2006.
[116] P Giannozzi, et al., J. Phys.: Condens. Matter 21 (2009) 395502.
[117] John Perdew, Kieron Burke, Matthias Ernzerhof, Phys. Rev. Lett. 77 (1996).
[118] J. Heyd, G.E. Scuseria, Matthias Ernzerhof, J. Chem. Phys. 124 (2006) 219906.